Escola de Postgrau
Universitat Autònoma de Barcelona

Departament de Fisica

Evaluation of the Field Gradient Lattice Detector

Treball de Recerca

May 9, 2008

Author:
David A. Watts

Supervisor/Tutor:
Prof. Enrique Fernandez

Tribunal:
M. Dolors Baro Marine
M. Pilar Casado Lechuga
Martine Bosman

0.1 Abstract

A novel Micro Pattern Gas Detector, named the Field Gradient Lattice Detector, has been implemented using technologies available to CERN's Printed Circuit Workshop. Numerous prototypes based on various materials were constructed in different geometries and their gain performance has been studied using ^{55}Fe and ^{109}Cd X-ray sources in Argon-CO_2 gas mixtures. Two axis (2D) prototype structures have been shown to provide stable gains of around 1000 while a 3D design, based on the same polyimide foils used in other MPGD elements, holds a gain of 5000 for 8.9keV X-rays even at high rates of 22kHz/mm^2. At a gain of 3100, the device has been tested up to 1MHz/mm^2 and shows no signs of degradation in performance. The energy resolution of the 3D-in-polyimide is modest, around 40% for 5.9keV X-rays and 30% if the source is collimated indicating a variation in gain over the 3x3cm^2 active area. Having the most promise for future applications, the 3D-in-polyimide design has been selected for testing with a custom-built readout electronics which uses an innovative front-end, the DP-GP5, for signal amplitude measurement and triggering. The front-end has been integrated with a portable data acquisition system which uses USB to communicate with a PC. Reading out the TOP and BOT electrodes of the 3D-FGLD, we have produced images of collimated radioactive sources and the accuracy of the readout as well as some discussion of charge sharing will be presented.

Contents

Chapter 1

Executive Summary

1.1 Introduction to CERN

Since March 2003, I have worked in Geneva, Switzerland, at the European Center for Nuclear Physics (CERN), the world's largest physics laboratory, and home of the Large Hadron Collider (LHC), a 27 kilometer circumference synchrotron which is scheduled to become operational by July, 2008. The LHC, located on average 100m underground between Lake Geneva and the Jura Mountains, will collide protons at energies of up to 7TeV, vastly beyond any other existing accelerators, in a regime of high-energy physics (HEP) so far not understood but in which theories have been formulated, such as string theory, super-symmetry, and M-theory. The LHC may also provide answers to some of the deepest mysteries of modern astrophysics, including the origin of dark matter, the mechanism of inflation, and the physics dictating the evolution of the universe in the earliest moments of the big bang. Giant detectors, ATLAS, LHCb, CMS, ALICE, TOTEM and LHCf, built in collaboration with the global HEP community and located in enormous caverns underground, will be the eye of the experiment looking to reveal new physics in the signatures of particles created in the collision points. The data rate expected from the millions of sensors comprising each detector is unprecedented - up to 320MB/sec for ATLAS - and an entirely new computing infrastructure named the Grid is being developed to support it. In addition to being by far the most complex and challenging machine ever built, the LHC project and its associated detector experiments is a tribute to our quest to probe the secrets of nature herself, representing the pinnacle of scientific achievement of the modern age.

1.2 Motivation of project

I began at CERN with an internship in the printed circuit workshop (TS-DEM-PMT) under the direction of Rui de Oliveira and it was there that I

became involved in a project to pursue an idea first proposed by Professor Louis Dick and Rui de Oliveira called the Field Gradient Lattice Detector (FGLD). I participated in the evaluation of the FGLD device in which I conducted studies of the detector's operating characteristics and performance as an ionizing radiation detector. I produced numerous FGLD prototypes in the workshop while applying various changes in the manufacturing procedure in order to optimize it for potential medical and industrial applications. Prototypes were fabricated in a variety of different materials and not all turned out to be as performing as others. It is the purpose of this text to present the results of the FGLD studies while highlighting some of the important aspects of the production techniques behind its construction. I feel privileged to have learned alongside Rui de Oliveira, whose ability in the field of photolithographic technologies remains unparalleled in the world, and who has been paramount to the development of Micro-Pattern Gas Detectors, now a standard workhorse of radiation detection systems used in research and industry. My hope is that at least some of his wisdom and artistry is transferred to the reader through the following discussion.

The first part of the thesis concerns the theory of gas detectors where I describe the physics of charged particle and photon interaction in matter followed by a discussion of charge transport and avalanche multiplication in gases. This will lead us into considerations for gaseous detector design and I will summarize the principles of operation of the Multi-Wire Proportional Chamber which serves as a reference point for all modern gas detectors. Upon this background I will describe the technologies behind Micro-Pattern Gas Detectors, highlighting the details of the photolithographic techniques used to produce them, specifically for the two most commonly used gaseous detectors in today's HEP physics experiments: the GEM and MicroMEGAS. I will continue by introducing the FGLD principle and the various methods employed to realize it in technologies available to the PCB workshop. The performance of selected proof-of-concept prototypes as a radiation detector will be presented. In parallel to the fundamental detector research on the FGLD itself, we set out to design a high-speed data-acquisition (DAQ) system capable of self-triggering for medical imaging applications. We evaluated a number of commercial multi-channel charge-sensitive preamp ICs from the Norvegian company, IDEAS, and integrated our selections along with a diode-protection IC to create a front-end design suitable for reading out the FGLD and other MPGDs. The result of our efforts is a unique front-end we like to call the DP-GP5 which is highly interesting in that it is self-triggering and has the potential for high-rate medical imaging applications. A brief description of its architecture will be presented along with the results of using the electronics for reading out a multi-channel FGLD specifically designed for this purpose.

Chapter 2

Theory of Gas Detectors

2.1 Charged Particle Interaction

High-energy charged particles, on their passage through matter, interact with the medium primarily through electromagnetic processes. Interactions arising from the strong, weak, and gravitational forces are orders of magnitude less probable and thus their effect in the context of this text will be ignored. In gaseous mediums, Coulomb interactions are the most probable and lead to ionization or excitation of the gas atoms along the path of the traversing particle. The ionizations result in the creation of electron-ion pairs which provide a signature of the particle's trajectory and form the basis of electronic detection.

When a high-energy charged particle passes through a medium it deposits energy mainly through Coulomb interactions with the atoms or molecules of the material. The energy deposited per unit distance, dE/dx, in a material having ionization potential I and electron density n, was first given by Hans Bethe in 1932 and follows the relationship

$$-\frac{dE}{dx} = \frac{4\pi}{mc^2}\frac{nz^2}{\beta^2}\left(\frac{e^2}{4\pi\epsilon}\right)^2\left[ln\frac{2mc^2\beta^2}{I(1-\beta^2)} - \beta^2\right] \tag{2.1}$$

where $\beta = \nu/c$, and the particle's velocity is ν and its charge ze. The electron rest mass is given in energy units and $mc^2 = 0.511MeV$.

In working with radiation detectors, it is convenient to speak of the reduced energy loss (or stopping power) where dE/dx is normalized to the density of the medium and expressed in units of $MeVcm^2/g$. In this framework, the minimum value of the stopping power is roughly equal to $2MeVcm^2/g$ independent of most material types. The minimum in energy loss occurs around particle energies of a few hundred MeV and at relativistic velocities, $\beta \to 1$, the energy loss increases only slightly. For this reason, charged particles above this level are generally called MIPs (minimum ionizing particles) and are often challenging to detect because of the low number of charge

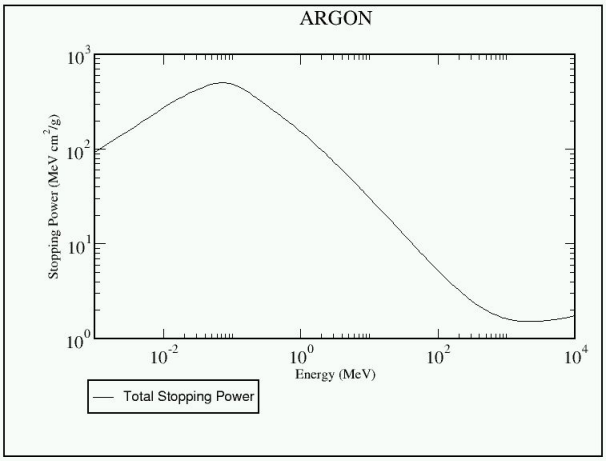

Figure 2.1: The reduced energy loss or stopping power of protons in Argon gas at STP.

pairs created in the detector medium.

The expression given in equation 2.1 is valid for heavy charged particles at energies above 300keV and below this value corrections are required. In practice however, sufficient experimental data exists to reasonably predict the energy loss for a given particle energy and detector volume. A database of the energy loss for protons and helium ions in many materials has been assembled by the National Institute of Standards and Technology (NIST) and is available for download from their website [1]. A plot of the stopping power for protons travelling through Argon gas at atmospheric pressure taken from the NIST website is shown in figure 2.1.

2.2 Photon interaction

Photons interact with matter only through electromagnetic processes but in contrast to charged particles, the interaction occurs as a single spontaneous localized event where the photon is either completely absorbed, or re-emitted after depositing some of its energy to the medium. Because the interaction is entirely probabilistic, the intensity of a beam of photons passing through a medium of thickness X can be stated simply as

$$I = I_0 e^{-\sigma N X} \tag{2.2}$$

where N is the number density of molecules in the medium and the cross-section, σ, is a measure of the probability of interaction in the medium. The cross-section, whose value depends on both the energy of the photon and the material, is best seen as the product of the probabilities for several

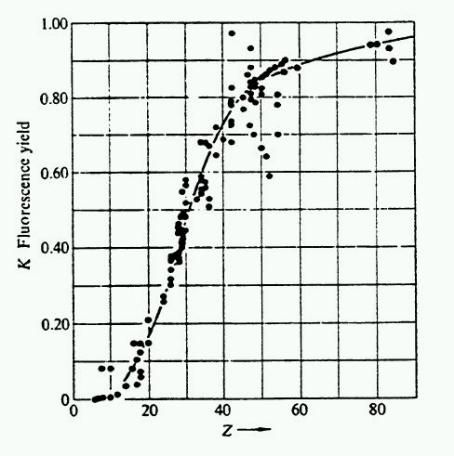

Figure 2.2: The fluorescence yield for different atoms as a function of atomic number.

competing processes: the photoelectric effect, Compton scattering, and pair-production.

At photon energies in the range of the atomic binding energies of atoms in the medium, the photoelectric effect dominates. Photons in this energy range are often called *soft X-rays*. In the photoelectric effect, the photon, having initial energy E_γ, is entirely absorbed by an electron from an atomic shell of the medium. The electron, now called a photoelectron, is ejected from the atomic shell with kinetic energy E_a, the difference between the photon energy and the binding energy of the shell. The ion successively de-excites by either fluorescence of a photon, having energy E_j, or by the release of an auger electron having kinetic energy E_j. The florescence photon can often leave the detector volume without interacting further and so only the net energy $E_\gamma - E_j$ is deposited in the detector. The probability for fluorescence to occur, expressed as the fluorescence yield, increases with atomic number Z as shown in figure 2.2 [2]. In Argon gas, it occurs only 15% of the time (as compared with roughly 90% in Xenon) and gives rise to an "escape peak" in the deposited energy distribution of events in the detector as we shall see later. Otherwise, the auger electron, which is released almost immediately upon ionization, is indistinguishable from the photoelectron, and the total energy, E_γ, is transferred into the medium. As the energy of the photon increases, the probability for interaction decreases rapidly. There is a tendency for the photon to liberate electrons held in deeper shells with higher binding energy and this gives rise to a series of characteristic edges visible in a plot of the photo-electric cross-section (see figure 2.3).

At energies above the highest atomic energy level of the medium, (so-called hard X-rays), the photon tends to interact through Compton scattering, a process in which the incident photon, having initial energy $h\nu$,

imparts only a portion of its energy to an atomic electron in the medium. The photon, scattered with an angle of θ, continues with a new energy $h\nu'$ such that

$$\frac{1}{h\nu'} - \frac{1}{h\nu} = \frac{1}{mc^2}(1 - cos\theta). \tag{2.3}$$

The energy transferred to the atomic electron, $E_T \equiv h\nu - h\nu'$, can assume any value down to 0 as $\theta \to 0$ and is at a maximum when the scattering angle is 180°. We can write the maximum transferable energy for the Compton process as

$$E_{T(max)} = h\nu \frac{2h\nu}{mc^2 + 2h\nu}. \tag{2.4}$$

This maximum appears in the energy spectrum if Compton scattering is present and it is recognizable as a continuous spectrum leading up to an edge characteristically lower than the observed or expected position of the photo peak.

At energies above 1.02MeV, equivilent to two electron rest masses, the photon or gamma ray can spontaneously create an electron-positron pair whose net kinetic energy increases along with the photon energy. The cross-section for pair production is much lower than for the photoelectric effect and Compton, and so gases, having a density three orders of magnitude lower than solids, are highly inefficient for gamma ray detection. To be efficient, gas detectors must either be operated at high pressure with high Z gases (like Krypton or Xenon) or must make use of thin layers of solid, high Z materials (like gold or lead) called "radiators" which convert the photon into other particles which can then be detected in the gas. One example of a detector that works on this principle is the Transition Radiation Detector which uses radiating materials in front of a gaseous detector. Upon passage of a high-energy gamma ray the radiator releases showers of soft X-rays which can then be detected through photoelectric absorption in the gas detector.

The total cross-section of photons in lead, including the separate contribution of all 3 of the processes discussed above, is shown in figure 2.3.

2.3 Electron and Ion Transport in Gases

In gases, the energy deposited by interacting radiation can liberate electrons with sufficient kinetic energies to ionize further atoms or molecules of the gas volume in a series of successive secondary interactions. Although the primary ionization electrons can assume a variety of kinetic energies depending on the nature of the interaction and even though the primary and secondary interactions are of a statistical nature, the total number of electron-ion pairs

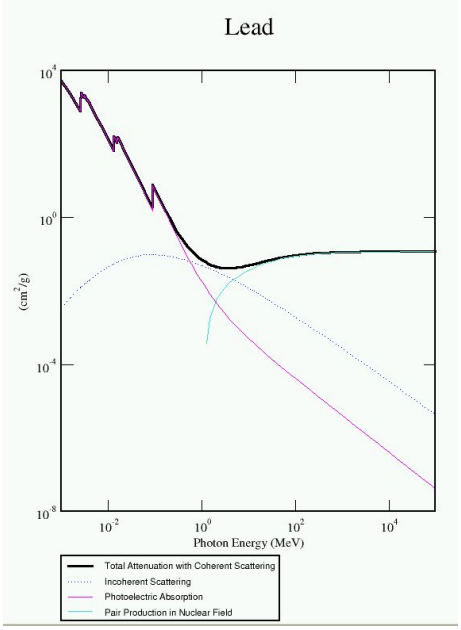

Figure 2.3: The total cross-section for photons in Pb.

produced after the passage of radiation, called the total ionization, can be calculated to a good approximation as simply

$$n_T = \frac{\Delta E}{W_i} \tag{2.5}$$

where ΔE is the total energy deposited and W_i is the effective energy needed to produce one pair. The relationship is convenient and provides a good estimation for most interactions assuming one takes care to account for any possibilities of secondary particles escaping from the detection volume, such as fluorescence X-rays or delta rays. Values for W_i have been obtained experimentally and a summary for several gases is given in table 2.1 along with values of the density, ρ, ionization energy, I_0, and stopping power dE/dx at atmospheric temperature and pressure.

Once in thermal equilibrium with the surrounding gas molecules, the electron-ion pairs are subject to diffusion which, in the absence of an electric field, can eventually lead to attachment of the electrons with the gas molecules, charge transfer of the ions to other atoms in the gas, or the recombination of ions and electrons either in the gas medium or on the walls of the detector. Recombination can be easily suppressed in gas detectors in the presence of electric fields which separate the electrons and ions and drift them towards electrodes for charge detection. The time scale for electron attachment to all noble gases and hydrogen is negligible but becomes important for other gases such as CO_2, O_2 and H_2O and in general depends

Gas	Z	ρ (g/cm^3)	I_0 (eV)	W_i (eV)	dE/dx MeV cm^2/g
H_2	2	8.38 x 10^{-5}	15.4	37	4.03
He	2	1.66 x 10^{-4}	24.6	41	1.94
Ne	10	8.39 x 10^{-4}	21.6	36	1.68
Ar	18	1.66 x 10^{-3}	15.8	26	1.47
Kr	36	3.49 x 10^{-3}	14.0	24	1.32
Xe	54	5.49 x 10^{-3}	12.1	22	1.23
CO_2	22	1.86 x 10^{-3}	13.7	33	1.62
CH_4	10	6.70 x 10^{-4}	13.1	28	2.21
C_4H_{10}	34	2.42 x 10^{-3}	10.8	23	1.86

Table 2.1: Properties of various gases common to gas detectors.

Gas	h	t (sec)
CO_2	6.2 x 10^{-9}	0.71 x 10^{-3}
O_2	2.5 x 10^{-5}	1.9 x 10^{-7}
H_2O	2.5 x 10^{-5}	1.4 x 10^{-7}
Cl	4.8 x 10^{-4}	4.7 x 10^{-9}

Table 2.2: Coefficient and average time for electron attachment in various gases.

on the electric field applied. We can understand why argon is a common choice as a primary constituent in gas detectors: it is inexpensive, has higher cross-section for interaction than helium or neon, and suffers no loss of electrons from attachment during charge transport. The non-zero attachment coefficient, h, for other common gas molecules common in the atmosphere explains why impurities in the detector volume should be avoided. A table summarizing the important parameters for the attachment process is given for several gases in table 2.2.

The drift velocity for ions, w^+, increases roughly linearly with the applied field and is usually written as

$$w^+ = \mu^+ E \tag{2.6}$$

where the ion mobility, μ^+, depends on the type of ion and surrounding gas composition, typically in the order of $1cm^2\ V^{-1}\ sec^{-1}$ in mixtures commonly used in gas detectors. During transport, collisions of the drifting ions can result in the transfer of their charge to other gas atoms or molecules having a lower ionization potential. In argon mixtures containing even only a few percent of molecular gases like isobutane or methyl gas, the charge transfer process is highly efficient and all drifting argon ions are quickly replaced by ions of the gas species having the lower ionization potential. This

is an important effect that we will discuss later.

Electrons, on the other hand, experience a non-linear response of the drift velocity w^- to the applied electric field. Despite a complex relationship, we can write a simplified one proposed by Townsend as

$$w_- = \frac{e}{2m} E * \tau(E) \tag{2.7}$$

where $\tau(E)$ is the mean time between collisions dependent on the electric field. The value of τ is also highly sensitive to the gas composition such that small additions of other gases can dramatically change the electron drift velocity. Above a certain value of electric field, the force of recombination can be overcome and the electrons are separated from their ion pairs and drifted towards the anode. Thermal elastic collisions with the gas molecules limit the electrons' acceleration and they move with a constant drift velocity in the direction of the electric field. If the gases are chosen correctly and the chamber is designed to be tight, the loss of electrons by attachment can be kept to a negligible level and all total ionization will be collected on the anode. Detectors which operate in this way are called *ionization chambers* and are useful for detecting heavily ionizing radiation such as alpha particles.

2.4 Avalanche Multiplication and Breakdown

The total ionization produced by a typical event in a gas detector is often several orders of magnitude too small for detection by charge-sensitive preamplifiers connected to drift electrodes in the detector. Fortunately, nature provides a mechanism for the amplification of the electrons through a process known as electron avalanche.

Since electrons have a mass much lower than that of the ions, in the presence of a strong electric field, they can achieve enough energy by acceleration along the mean free path between collisions to create processes other than thermal elastic collisions. When the electron's energy is higher than the ionization potential of the gas, collision can result in ionization and the creation of a new electron-ion pair. The newly created electron, in turn accelerated by the electric field, can repeat the process of ionization in a repeating cascade known as avalanche multiplication. The process is most generally described using the first Townsend coefficient, α, defined as the number of electrons produced in the path of a single electron having travelled 1cm in the direction of the field [3] such that the total number of electrons produced by n primaries over a distance of x is

$$n = e^{\alpha x} \tag{2.8}$$

De-excitation photons can also be released in the avalanche and can lead to further charge-pair creation. Although the drift velocity of the electrons

follows a complex behavior, the multiplicity of the avalanche process can be tuned by a careful adjustment of the electric-field and the right selection of the gas mixture. While pure noble gases are only either excited or ionized, other gases, particluarly polyatomic ones, can also be excited into higher rotational or vibrational modes do so by absorption of the photons produced in the avalanche. Addition of such a gas, also known as a *quencher*, has the effect of limiting the avalanche process before it races out of control by the absorption of the photons produced. Polyatomic gases also have an additional quenching effect important to chambers operating in avalanche mode. When a drifting ion reaches the cathode to recombine with an electron, energy is released which can often take the form of an emission of an electron from the metal surface. Since the electron will in turn drift and experience amplification, the chamber will be caught in a feedback loop. Polyatomic ions however, usually dissociate with the energy released upon neutralization instead of provoking a release electron from the cathode. If the polyatomic gas has also a lower ionization potential than the primary gas constituent, then all ions arriving on the cathode will be of the polyatomic species which dissociate and propagation of the avalanche will be suppressed.

In the right gases and over a range of applied field, the avalanche multiplication factor, or gain G, can be made constant to a good degree independent of the number of primaries and their path of arrival under the influence of diffusion. In this condition, the collected charge after amplification is *proportional* to the primary charge deposited in the detector from the ionizing radiation and detectors who operate in this region are called gas *proportional chambers*.

At very high values of fields, and in regions of high field gradient, space charge effects from the large number of electron-ion pairs created in the avalanche can distort the local field leading to non-proportional operation. Observed is a kind of saturation of the total amount of charge collected on the anode and operation in this region is useful for simple pulse counting but not for energy measurements. Working on this principle is the Geiger-Muller tube, invented by Hans Geiger in 1908 and improved by the help of Walter Muller in 1928 who added alcohol vapor to the gas mixture which acts as an effective quencher.

At extreme fields, especially in the absence of a quencher, the massive build-up of charge carriers localized in a single region effectively add further to the multiplication process. The avalanche extremities grow in size and extend themselves towards the anode and cathode to form a *streamer*. If the streamer grows to touch both the anode and cathode, a current can flow along the conductive plasma channel of the streamer and the short-circuit is called a discharge or breakdown which is usually dangerous for the survival of the detector and electronics. The limit of gain before breakdown and discharge is known as the *Raether limit* and occurs when

$$\alpha x \sim 20 \tag{2.9}$$

where x is the gap distance and α is the inverse of the mean free path for ionization also known as the first Townsend coefficient. Because the electrons in the avalanche have a distribution of energies and it takes only a few electrons to create breakdown, the Raether limit can be depassed even at gains of only 10^6 and this sets a practical upper limit on the maximum achievable gain in gas detectors.

2.5 Charge collection and electronic readout considerations

Modern gas detectors used in particle physics research and applications seek to measure the primary energy deposited by radiation and to localize the interaction point in the gas volume. By tuning the field, the primary ionization pairs can be drifted uniformly, without losses or amplification, such that the spatial signature of the event - whether it's a track from a charged particle or a cluster from a converting X-ray - is preserved albeit any loss of resolution caused by the effects of diffusion. Finely segmented electrodes in which each is equipped with a fast preamplifier can provide information about the spatial distribution of the arriving signature. Electrodes are often held in a planar configuration for simple reconstruction and spaced evenly at small distances to acheive an adequate resolution. At small distances primary ionization clusters can be shared over several electrodes and due to electronic noise constraints, avalanche multiplication is the only solution for the detection of often tiny amounts of primary charge (about $40e^-/cm$ for MIPs).

Fundamental to electronic detection is the collection of electrons on the positively biased electrode, the anode, and the recombination of ions on the surface of the negatively biased electrode, the cathode, which forms the electronic signal. The voltage that one can measure between on an electrodes having capacitance C is given by

$$V = \frac{ne}{C} \tag{2.10}$$

where n is the total number of charge pairs collected and e the electron charge. Signal formation, however, is dynamic in time since the current induced in the electrodes mirrors the movement of the charge drifting between them. An avalanche occurring near the surface of the anode will result in a fast rising signal from the collection of the electrons followed by a gradual decay from the slower drift of the ions towards the cathode. Also, the passage of charge in proximity of an electrode will produce an induced signal

even if the net collected charge is zero. This effect is exploited in some detector designs equipped with ultra-fast charge-sensitive, or current-sensitive preamplifiers.

2.6 Proportional Chambers

Gas Proportional Chambers are gaseous detectors operating such that the total number of charge pairs produced in avalanche and collected in the anode is proportional to the total ionization, by a constant factor G. Since modern detectors require finely segmented anodes and the charge is shared over several electrodes, the gain must also be constant for all electrodes, regardless of where the radiation interacted in the gas volume. To do this, the amplification zone should be separated from the interaction volume whose job is only to drift the charges towards the readout. The amplification is confined to a region very close to the readout plane such that incoming electrons only have a short distance over which to multiply before being promptly collected. If the gain is known, the total collected charge can be used to measure the energy deposited and to give an indication about the type of radiation that interacted in the drift volume.

The concept of the Multiwire Proportional Chamber, shown schematically in figure 2.4 and invented by Georges Charpak in 1968, makes use of narrow conductive anode wires, regularly spaced and often in orthogonal axes, which form the segmented anode plane and yield the position information [4]. Operating in the proportional region, the avalanche multiplication occurs very near the surface of the wires, whose diameters range in the tens of microns, where the electric field increases rapidly as $1/r$. This results in a fast-rising signal induced in the wire and a limited region for avalanche that all electrons drifting through the detector volume experience equally. The wires are held under tension and evenly spaced apart in a plane separated from the drift anode in order to provide a uniform field configuration. Charpak eventually recieved the Nobel prize in 1992 for his invention and wire chambers, forty years later, are still used extensively in high-energy physics and industrial X-ray scanning systems.

2.7 Modern Micro-Pattern Gas Detectors

Since the invention of the Multiwire Proportional Chamber (MWPC), there has been a great deal of interest in the field of gaseous detectors and much of the knowledge concerning gas detector operation that we have for a variety of different gases, owes to research surrounding it's conception. Some years later, a new design for a proportional gas chamber was introduced by A. Oed called the Micro-strip Gas Chamber or MSGC [5]. It has a similar structure to the MWPC, only instead of wires, two sets of anode and

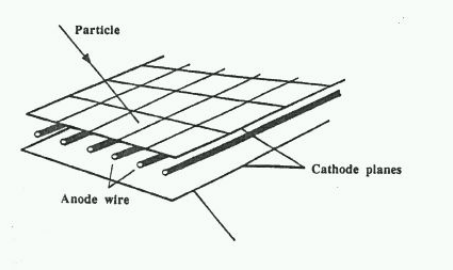

Figure 2.4: A schematic representation of a proportional wire chamber.

cathode strips, produced on a layer of glass substrate, provide the amplification of charge in a region of high electric field gradient focused near the edges of the strips. Though research on the device was soon abandoned because of problems with discharges, the invention is invaluable as an example of applying an old concept using modern technology. The idea to replace the floating wires, prone to mechanical distortions when under voltage and time-consuming to mount mechanically, was the beginning of a new approach to proportional gas detector design. The lessons learnt from trials of the MSGC eventually paved the way for an entire new class of detectors now known collectively as Micro-Pattern Gas Detectors (MPGDs). It was demonstrated that by using photolithographic technologies, one could create uniform layers of conductive strips in virtually any desired shape and size on a rigid substrate robust and easy to handle and mount into useful detector assemblies. Furthermore, in a important conceptual development by Yanis Giomataris, came the idea to separate the amplification mechanism from the segmented readout plane. A perforated electrode, help precisely by a patterned insulating layer only several hundreds of microns from the readout plane could effectively pull electrons from the drift region into a contained region of high electric field for amplification and collection. The Micromegas (MICRO-MEsh GAs Structure) detector makes use of this idea in which a thin metallic foil or mesh, highly perforated by a matrix of holes, is held at a precise distance above a segmented readout plane by insulating spacers whereby a high electric field is created in the gap between mesh and readout such that electrons drifting towards the mesh in the interaction volume are steered through the mesh, amplified and detected on the readout plane [6]. Ions produced in the avalanche process are also mostly absorbed on the mesh due to their low mobility and the result is a faster signal than that of Multiwire Proportional Chambers. Also, the high-density perforation of the mesh, made possible by the high resolution of photolithographic techniques, results in a very uniform amplification over the surface of the detector and thus a high energy resolution. A schematic representation of a Micromegas gas detector is shown in figure 2.5. The spacing between readout and mesh is kept small to limit the avalanche length, typically on the order of hun-

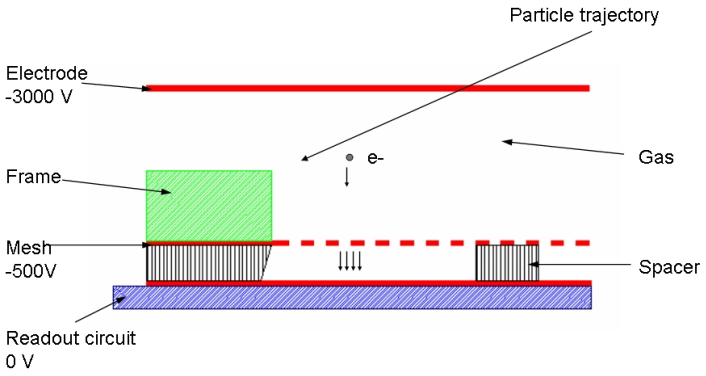

Figure 2.5: A schematic drawing showing a Micromegas gas detector in operation and typical biasing values. The mesh is usually held around 150μm from the anode plane resulting in a high electric field which causes the avalanche multiplication.

dreds of microns. The beauty of the Micromegas idea is that it allows the production of the mesh to be completely separate from the readout board which can be made of strips or pads in any desired geometry. A schematic drawing of several types of readout board, showing the method for interconnecting the strips or pads in one, two, three axes, or in a pixilated matrix, is shown in figure 2.6.

Still, single gap detectors, such as the Micromegas described above, suffer one important drawback: since the amplification occurs in a single stage gap between the mesh and readout, in the unfortunate event of a discharge, all of the charge will be absorbed entirely by the readout anodes as the electrodes release their stored energy upon short-circuiting. The resultant current surge in the input of the preamplifier, many orders of magnitude larger than signals of interest, can be fatal to the electronics. What's more, the discharge is also harmful to the thin copper surface of the readout strip or pad. In a clever idea proposed by Fabio Sauli, the region of high electric field needed for amplification is confined to an independent element which can be positioned away from the readout by the order of a few millimeters. The amplifying element, named the Gas Electron Multiplier (GEM) [7], comprises two electrode layers on two sides of an insulating foil, perforated by a high density of micro-holes (70μm diameter) spaced apart at regular intervals (120μm). When a voltage is applied across the electrodes a high electric-field is produced in the holes which provides the avalanche multiplication. A moderate field between the underside of the GEM and readout, also called an extraction field, is used to extract the electrons amplified by the GEM and to transfer them towards the readout. In correct operation, discharges should occur only between the GEM electrodes where

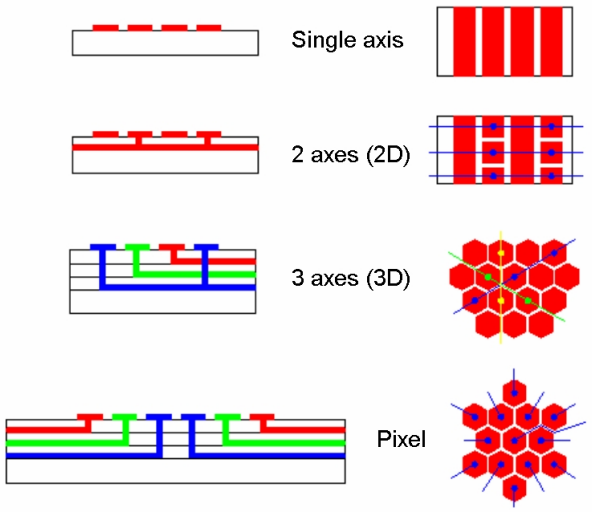

Figure 2.6: A schematic drawing of various possible readout designs for MPGDs.

a portion of the total charge is absorbed by the GEM itself. A schematic representation of a GEM mounted in a gas detector assembly is shown in figure 2.7.

The GEM can be thought of as a kind of matrix of electrostatic micro-lenses which focuses the ionization charge inside the holes. The electric-field configuration inside a single GEM hole is shown in figure 2.8. Incoming electrons will follow the field lines into the region of high-electric field and be amplified independent of their initial distribution in the drift volume, a necessary condition for good energy resolution. Because the profile of the hole - and thus the field configuration - is symmetrical, electrons are spread out as they exit the GEM structure much in the way as they come in. The

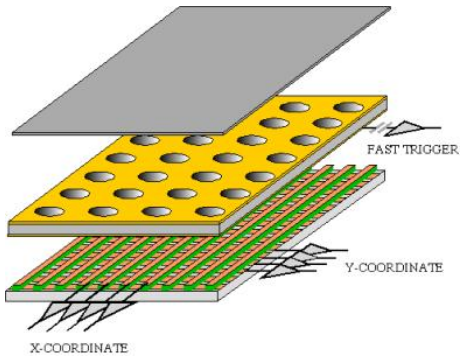

Figure 2.7: Schematic drawing showing a single GEM gas detector configuration.

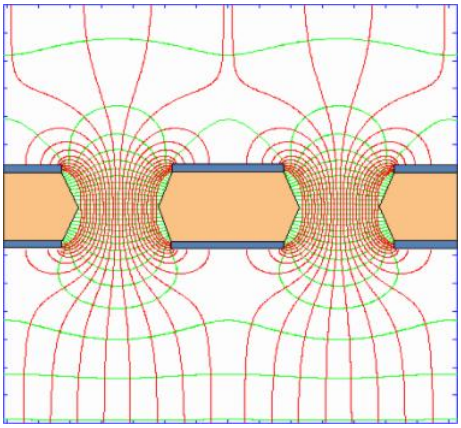

Figure 2.8: The electric field at the center of the hole of the Gas Electron Multiplier. Simulated with Garfield.

exiting charge cluster will thus have a wide spatial distribution and will be collected on the readout plane by more electrodes than in a single gap device. This is beneficial both for the life of the detector elements and the electronics since the entire charge in discharge is not focused onto only a few anode strips as in the Micromegas or the MWPC. Although it seems that this charge spreading would result in a poorer spatial resolution, it actually improves it when a center-of-mass fitting algorhythm is used to find the center of the distribution. In large area applications where the number of electronic channels must be limited for financial reasons, detectors based on GEMs using relatively large anode pads still yield accurate position reconstructions since the charge is shared in several channels. In one application using square anode pads of 2mm, resolutions of 100μm have been achieved [10].

As the GEM foil itself is self-supporting and only serves to amplify the charge, there is no restriction for stacking GEMs to increase the amplification. Of course, the maximum effective gain is not limitless and the addition of each GEM increases the diffusion of the charge leading to an eventual loss of position resolution. Still, the use of multiple GEM foils allows operation at voltages less prone to discharges since the work of amplification is shared between each of the GEM structures. Each GEM operates at a lower gain and the total effective gain is just the product of each contribution. Triple-GEM structures are widely used in current HEP applications because of their very low discharge probabilities and high achievable gain (up to 2x10^5 in Ar:CO_2 gas mixtures). They also have a further advantage over other detectors using a single amplification stage. Because the mobility of ions is much lower than electrons, ions produced in each stage of amplification and moving towards the drift cathode are largely absorbed on the bottom layer of the upper GEMs and thus do not feedback into the drift region. This is important for achieving high spatial resolution since ions in the drift volume

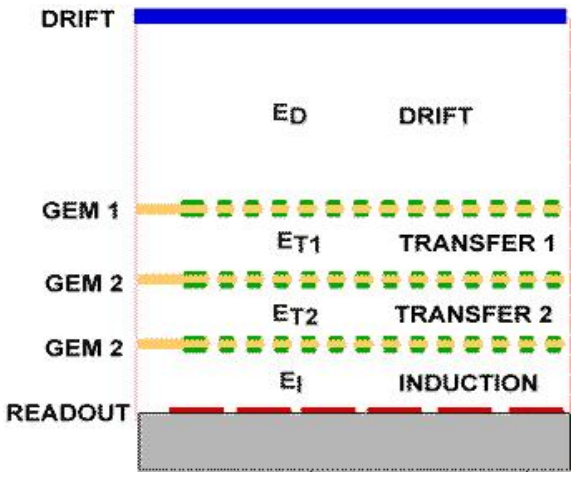

Figure 2.9: Schematic drawing of a triple-GEM detector.

effectively modify the field configuration leading to distortions of the drifting ionization. This is especially critical for Time Projection Chambers (TPCs) which use very large drift distances (up to several meters) and precise timing information in order to reconstruct the third dimension of the ionization event; even small field distortions can lead to large errors in the position reconstruction and thus ion feedback must be kept to a minimum. Triple-GEM detectors used in a standard configuration have typically 2% effective ion feedback, defined as the ratio of ions collected on the drift cathode to the electrons collected on the readout anode plane. A recent work describes the use of the uppermost GEM foil as a gate to block the ions which could reduce the value significantly to only 10^{-4} [11]. Figure 2.9 shows a schematic drawing of a triple-GEM gas chamber.

Chapter 3

Micro-pattern Gas Detector technologies

3.1 A quick tour of the CERN PCB Workshop

The European Center for Nuclear Research is host to a number of research groups, services, and facilities, on the cutting edge of technology. From detector construction, electronics design, CERN has all the expertise and infrastructure to meet the complex needs of the LHC and its associated detector experiments. The PCB Workshop, located on the CERN Meyrin site, is no exception. Although responsible for mostly small-volume production of standard printed-circuit boards, the workshop has the capacity for more exotic technologies, such as: thick-and-thin film printing, PCB, flex, and hybrids. Furthermore, the workshop utilizes a minimum of automated machinery common to production-line PCB manufacturers, and it does so with a kind of hand-crafted artistry unparalleled in the industry.

3.1.1 The Chemical Via method

The CERN PCB Workshop is unique for its development of a process called the ChemcialVia [12]: a entirely chemical method of etching polyimide (also known as Kapton) and used for the production of Micro Vias, micro interconnections between layers of PCB in ultra-high-density circuit boards 3.1. As it is an entirely chemical procedure, etched profiles of any size or shape can be obtained in a single straightforward manufacturing step in which a patterned polyimide foil is passed through a series of chemical baths. Although it can be used to produce extremely tiny interconnections between layers through the metallization of the holes, its importance in the context of this text lies in possibilities for high-definition shaping of the polyimide foils. Structures such as segmented readout electrodes and micro-mechanical foils - which form the constituents of MPGD elements - become technologically

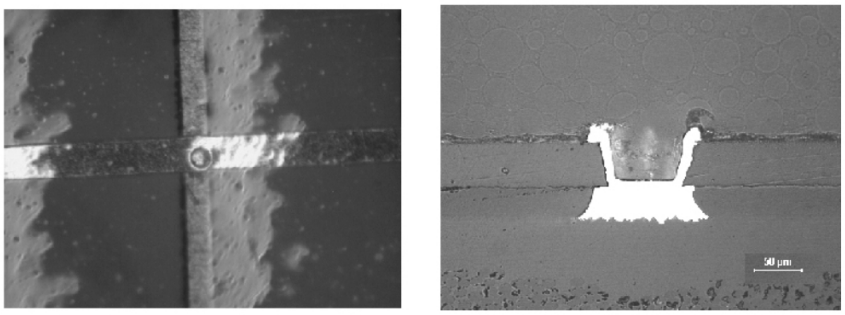

Figure 3.1: SEM images of a microvia.

feasible.

3.1.2 MPGD technologies

Micro Pattern Gas Detectors (MPGDs) are devices which operate on the same principles as Proportional Wire Chambers, yet which do so by implementing micro-patterned structures produced from base materials common in PCB manufacturing. Segmented readout electrodes and micro-meshes can be built up in a series of laminations of copper-clad photo-imagable materials, followed by the chemical removal of the insulating material between the copper layers through image transfer, development and/or etching. Standard base materials include copper-coated rigid board, double-sided copper-clad polyimide foils (also known as Kapton and used in flex technologies), and metallic foils which can be glued to a rigid board. Newer materials include micro-meshes and photo-imagable solder mask. In all constructions, the insulating support provides mechanical rigidity for the electrodes and since tolerances on the thickness of materials and processes is high in the industry (less than 3μm over surfaces of 50x50cm), an accurate spacing of the layers is guaranteed. This is one of the main advantages of MPGDs over wire chambers which suffer from field non-uniformities produced by the forces created on the wires under electric field. The uniformity of the electrode spacing and the precision of the production techniques has allowed MPGDs to far surpass the performance of older gas detectors. Adding to popularity, PCB technology is relatively inexpensive, and materials are widely available from commercial vendors. Given also the freedom one obtains in applying the various techniques of photolithography to allow an almost limitless possibility for new designs it is not hard to appreciate why MPGDs have gained some much attention in the detector community in recent years.

Many innovative designs for MPGDs have strung into life following the original innovation embodied in the Micro-Strip Chamber. It was one of the first MPGDs given serious attention but was later replaced by the more

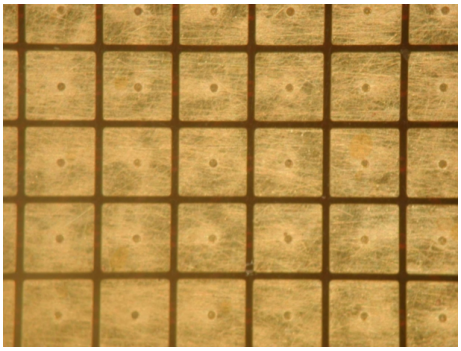

Figure 3.2: A pixilated readout board. The pixel pads are 150μm square.

robust Gas Electron Multiplier and the Micromegas. Other types of MPGD soon followed suit including the Microgroove, and Microwell, to name a few. In addition, readout boards made of strips in two or three axes and including pixilated anode planes were developed to be used in parallel with amplifying structures. An example of a pixel readout produced in the CERN Workshop is shown in figure 3.2. Each pixel is 1mm by 1mm square and routed to a separate pin of a connector outside the active area. Currently there are many different types of MPGDs used in high-energy physics research, astrophysics, and nuclear medicine and imaging. Though still in use in legacy systems, primarily in X-ray scanning systems in the food and security industries, the Proportional Wire Chamber has been entirely replaced by the newer generation of gas detectors, the MPGDs. An interesting fact is that, despite the enormous variety of innovative designs which have sprung to life in recent years and their widespread use in scientific research around the world, MPGD elements are still predominantly produced in a single place, the CERN PCB Workshop.

3.2 GEM

3.2.1 Fabrication Overview

The Gas Electron Multiplier (GEM) consists of a double-sided copper-clad polyimide foil of 50μm thickness and perforated by a high-density of regularly-spaced conical holes with typically 80μm diameter. A SEM image of a GEM foil produced at CERN is shown in figure 3.3.

In order to function optimally, several constraints on the manufacturing need to be observed. The alignment of the hole image on both sides of the GEM and the specific chemistry used in the polyimide etching process play a crucial role in determining the shape of the hole and thus the electric-field configuration. Figure 3.4 shows different profiles obtainable through different chemical etching. In most etching techniques, by the time the etching

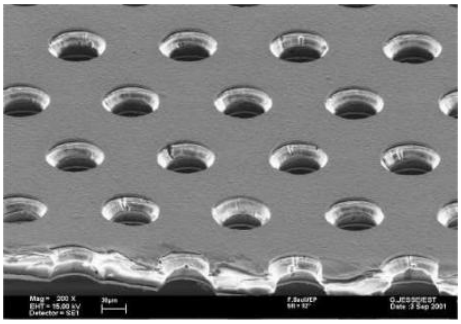

Figure 3.3: A SEM image of a Gas Electron Multiplier produced at CERN.

is complete some the insulator beneath the copper has also been removed giving the over-etched profile shown in the upper most example. The lowest profile is the standard for drilling or plasma etching while the preferred profile is the so-called *double-conical*, shown in the middle example, which both facilitates cleaning after etching and provides optimum amplification characteristics. Many detailed studies on GEM detector using one, two and three foils have been conducted to optimize the manufacturing process [13]. The result is that GEM is now a standard product for the CERN workshop with sales of up to 1000 foils per year in the HEP community. GEMs with active areas of up to $40x40cm$ are routinely produced and large areas, bigger than $50x50cm$, will very soon be feasible. Developments are ongoing to implement the GEM structure in new materials; ThickGEM and RETGEM are some recent examples [14] [15]. At the time of writing, other laboratories trying to produce GEMs are still only able at best to match the performance and uniformity now standard with those produced at CERN [16] [17] [17] [18].

3.2.2 Electrode segmentation

Though an additional step of patterning either side of the perforated GEM foil, each copper layer can be segmented into any series of electrically isolated electrodes. In large-area GEM foils, the upper plane is patterned into segmented electrodes in order to reduce the capacitance of each sector with respect to the lower plane. This limits the energy stored in the GEM foil and thus the charge released upon discharge and breakdown which can be harmful both for the GEM foil itself and for the readout electronics. Segmentation of the GEM foil is now extensively used in GEM designs larger than 10x10cm. Figure 3.5 shows the segmented 30x30cm GEM for the COMPASS (COmmon Muon and Proton Apparatus for Structure and Spectroscopy) experiment [19].

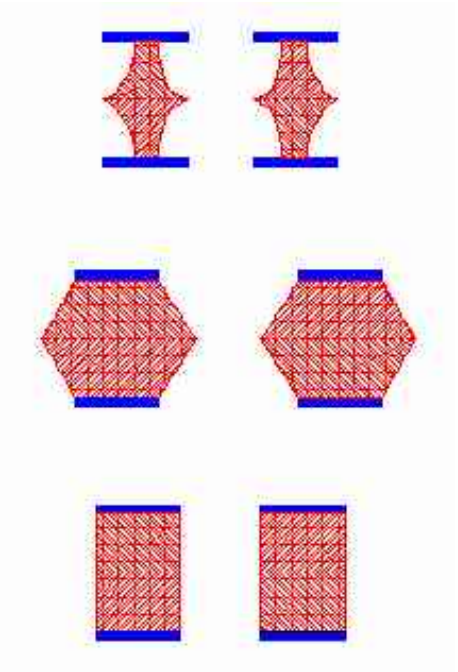

Figure 3.4: Different hole profiles obtainable through the polyimide etching process. The double-conical profile is the one used for optimally performing GEMs.

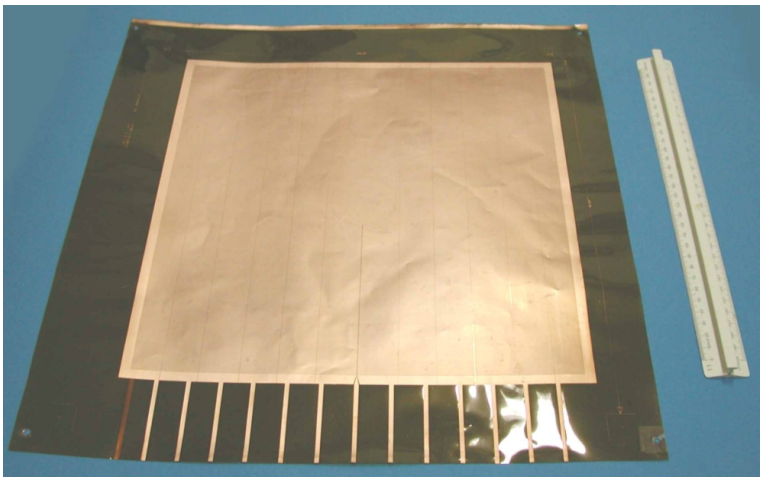

Figure 3.5: A 30x30cm GEM for the COMPASS experiment in which the upper electrode is segmented into 13 sectors.

3.2.3 Quality control of GEM foils

All GEM foils produced at CERN, before leaving the workshop, are tested under voltage in a clean room and the voltage limit before inducing discharges serves as the primary quality-control parameter. They are required to hold a minimum of 600V in dry air (20% RH) with less than 10nA of leakage current for a period of several minutes with very few discharges. GEMs that don't hold to this criterion are inspected for defects or contamination and can often be recovered using further chemical treatments or repeated cleaning. It has also been noted that during periods of high-humidity, GEM foils can be simply un-testable in open air; repeated discharging or leakage currents even at low voltage give the impression of a defective GEM. Annealing the GEM at around 80 °C for one hour and testing in a dry environment often cures the problem. As such, it is important to be aware of the humidity in the testing environment.

On arrival to the physics lab, GEM detectors are handled only with gloves and in the cleanroom where they are mounted into useful detector assemblies. Contamination is a constant threat for the survival of the detector and a rigorous assembly procedure involving repeated discharge tests of all GEM foils is generally practiced and is crucial in preventing avoidable and costly mishaps. The documentation of triple-GEM chambers for the COMPASS experiment serves as an excellent example of a well-planned GEM assembly procedure [20].

Occasionally, discharges during the testing process lead to permanent leakage currents which are non-repairable even with drastic intervention. From a naive perspective, inducing discharges across GEM foils should thus be avoided as much as possible. However, by following a few intuitive guidelines when applying voltage, such as to limit the current with a large series resistor, typically 10MΩ, the discharge behavior can be a useful indicator of the GEM's quality and potential performance. By observing whether the discharges occur in a single location or spread out over the foil, one can gain insight into the nature of a problem. Repeated localized discharging usually signals a serious problem of defect or contamination whereas a few sporadic and randomly-distributed discharges are a common phenomenon while ramping-up the voltage, especially after cleaning, or after a long period of storage in a dusty environment. It is also observed that GEM foils display a tendency to spark in the early part of their life probably due to micro-spikes in the copper left-over from the etching process though a light micro-etching followed by chemical cleaning is often used to reduce this effect. Applying a modest voltage for extended periods of time and allowing the detector to discharge repeatedly in a process known as *conditioning* is often benificial and employed commonly by GEM users.

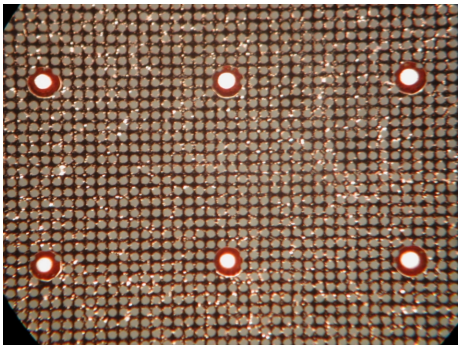

Figure 3.6: Microscope view of the active area of a MicroMEGAS made from a copper-clad polyimide foil. The holes of 25μm diameter are arranged in a regular matrix at 50μm pitch. The support pillars are repeated every 1mm.

3.3 MicroMEGAS

The same copper-clad polyimide foils used for GEM fabrication are also used in the production of Micromegas which can be described simply as micro-meshes precisely suspended above segmented readout electrodes at distances on the order of hundreds of microns. Fabrication of the micro-mesh involves transferring the image of the mesh or grid into the copper of a single-sided foil whereupon the polyimide is almost entirely etched away save a matrix of evenly-spaced *pillars* which serve as the mechanical spacers. The micromesh can then be mounted and held precisely over the anodes readout plane. Both the conductive mesh and the polyimide spacers can be made in a variety of different patterns and shapes and an example of one geometry is shown in figure 3.6 built in the CERN workshop for the CAST (CERN Axial Solar Telescope) experiment [21].

3.3.1 Micromegas made from bulk mesh

Recently, there has arisen an interest to produce the Micromegas structure using a finely woven conductive mesh. To produce a Micromegas from this bulk material, the meshes are laminated in sheets of photoimagable solder mask (used in standard PCB production) which is then patterned to provide the mechanical support for the delicate mesh by means of spacers similar to those in classic Micromegas. Large area layers of mesh and polymer mask can be laminated directly onto a prepared rigid readout structure and the spacers formed in a single photolithographic step providing for highly economic and straightforward manufacturing. Further motivation for the idea lies in that the meshes are low-cost and that the pattering of the insulator is done by a single image transfer and development step. No etching

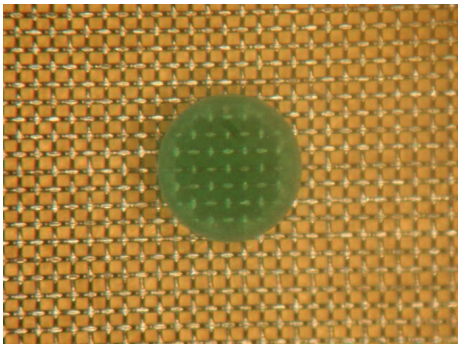

Figure 3.7: Microscope view of the active area of a MicroMEGAS made from bulk mesh material. The green "dot" in the center is a pillar of solder-mask material patterned at regular intervals to provide support for the mesh.

of polyimide is necessary as in the classic Micromegas design. Figure 3.7 shows a microscope image of a prototype detector made in this technology. Initial evaluation of the Micromegas in bulk detectors has been performed by a CERN/CEA-Saclay collaboration [22] on prototypes having 9x9cm^2 active area. Recently, large-area Micromegas in bulk, up to 27x26cm^2, have been produced in the CERN workshop made of a stainless-steel mesh having 19μm diameter wires interwoven at 59μm pitch for application to large TPC design, notably in the T2K experiment [23]. Stable gains of up to 10^4 and an energy resolution of 11% have been achieved with these detectors in Argon-Isobutane gas mixtures.

Chapter 4

FGLD: The Field Gradient Lattice Detector

4.1 Introducing the FGLD idea

During the time of the developments leading to the rise of MPGD technology, a new concept for MPGD realization was proposed by Prof. Louis Dick and Rui de Oliveira of the CERN PCB Workshop.

They set out to create a detector based on a matrix of electrically isolated electrodes (or strips) stacked in 2 or more layers which combine in a single micro-pattern construction the two fundamental elements of a MPGD: the gas amplification mechanism and the segmented readout.

The electrodes of each layer, separated by patterned insulating base materials, would be biased in a reverse cascade configuration such that electrons produced in the gas volume from ionizing radiation and drifted towards the detector surface are focused into regions of high electric field gradient within the detector and subsequently amplified through avalanche multiplication and then collected on the final electrode layer. The positive ions produced by the charge-amplification process, would be also collected on the upper electrode layers resulting in a rapid signal formation and a low level of ion feedback to the drift volume. The strips would be aligned at orthogonal directions in order to minimize the capacitance between layers thereby maximizing the measurable signal. By interpreting the distribution of the charge collected on the strips of each electrode layer placed at orthogonal directions, the trajectory of the original ionization event in the detector volume can be reconstructed.

The combination of the amplification mechanism and the readout brings us back to the problem of the MSGC and Micromegas: namely that all the charge created upon discharge in the amplification region is collected by only few electronic channels. The FGLD design seems to have abandoned conventional wisdom, however, it was thought that the capacitance of the

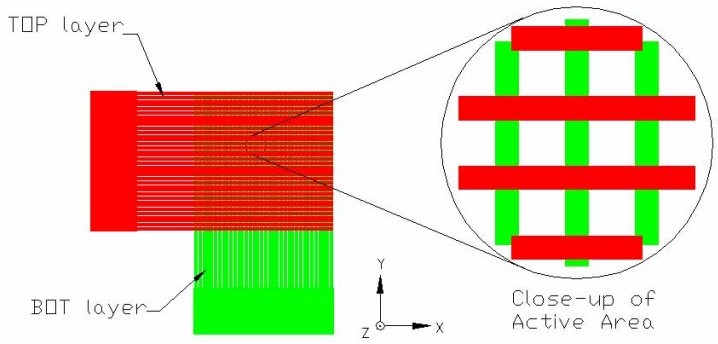

Figure 4.1: A drawing of proposed electrode images for a 2D FGLD proof-of-concept design.

individual electrode strips of each layer would be so small that the total energy released, which varies with the square of the capacitance, would be orders of magnitude lower than the portion of the energy absorbed in the readout from a discharge across a GEM foil with segmented electrodes.

To illustrate the FGLD principle in its most simple construction, consider figure 4.1, a sketch of the film images needed for producing a 2D (two-axis) FGLD in which the patterned electrode strips are arranged at 90° with respect to each other. In this proof-of-concept design, the strips of each layer are connected together electrically outside the active area for ease of applying the voltage and testing of the principle.

A drawing for the images needed for a three-axis, 3D-FGLD, proof-of-concept design is shown in figure 4.2. The electric field configuration established upon biasing the layers of the detector in a cascading voltage configuration would serve to focus the electrons into the structure for amplification and facilitate collection on the final electrode. The electrodes in each layer are aligned to create regions of mutual cross-over alongside empty regions or *holes* similar in geometry and dimension to those of the GEM. With the right geometrical parameters and the right biasing, the effective gain should be mostly uniform regardless of the arrival path of the incoming drifting primary ionization.

4.2 FGLD technologies

A wide variety of FGLD structures were made in the PCB workshop using different base materials and a general description of the architecture of the most noteworthy designs follows.

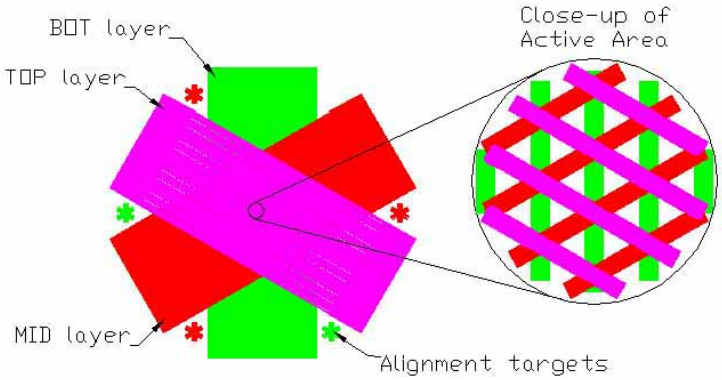

Figure 4.2: A drawing of proposed electrode images for a 3D FGLD proof-of-concept design.

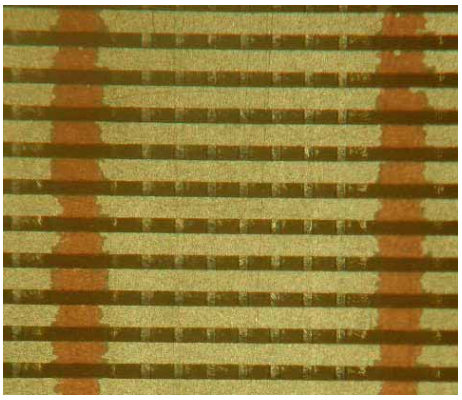

Figure 4.3: Closeup view of the 2D-FGLD microstructure made from copper foils and epoxy resin.

4.2.1 2D FGLD in epoxy

The 2D FGLD architecture was implemented using copper foils and epoxy resin. In the production procedure, strips forming the BOT layer are patterned on a copper foil on a standard rigid copper-clad board and subsequently buried under a uniform layer of epoxy resin glue. A single copper foil is then laminated onto the glue and cured at 180°C in a press. The TOP electrode is then patterned into the upper copper foil and the epoxy glue removed by etching, all but for selected regions which provide support for the upper strips. No glue remains between the electrodes in the active area. A microscope image of the 2D FGLD in epoxy resin is shown in figure 4.3. The pitch between strips is 200μm and the TOP and BOT strips are 120 and 40μm, respectively.

While the BOT layer strips are fixed to the rigid board, the strips of

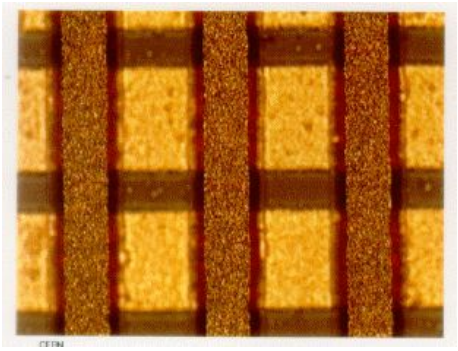

Figure 4.4: Microscope view of a generic XY readout board used in GEM-based detectors. The

the TOP layer are only fixed by narrow regions of epoxy resin spaced at regular intervals of several millimeters and visible as the vertical red lines in the microscope view. It was recognized early on that this leads to deformation of the TOP strips when biased under voltage. Attempting to reduce the distance between regions of remaining epoxy would only create more dead zones in the active area. Because epoxy glue etching process is isotropic, that is, the acid etchant evenly attacks the glue at all angles, it is nearly impossible to hide the support structures in a region beneath the TOP electrodes. Although this design was able to produce signals from ^{55}Fe and ^{109}Cd X-ray sources seen on the scope, the energy resolution was very poor and discharges were frequent. For these reasons, interests turned towards other materials and no results of the 2D-FGLD's performance will be presented here.

4.2.2 3D FGLD

The FGLD can be implemented using copper-clad polyimide foils 50μm thick, identical to those used in GEM, Micromegas, and in 2D, 3D, and PIXEL readout production. The anisotropic nature of the ChemicalVia polyimide etching chemistry is what is characteristically different about structures based in polyimide as opposed to epoxy resin. The etchant attacks the polyimide non-uniformly and with the right chemistry and skill, the polyimide if left exactly beneath the patterned copper layer. Narrow strips of copper, having widths on the order of the polyimide thickness, 50μm, can be supported by matching strips of insulator. The method is used to produce 2D readout boards (see figure 4.4) commonly found in GEM-based detectors. Taking this technology in hand, we implemented the 3D FGLD architecture.

In the production procedure, the electrode images: TOP, MID and BOT, are transferred into the copper surfaces of two foils and glued to create a

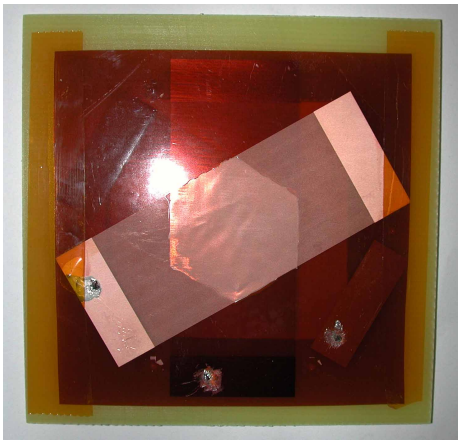

Figure 4.5: A 3D-FGLD prototype based on patterned polyimide foils.

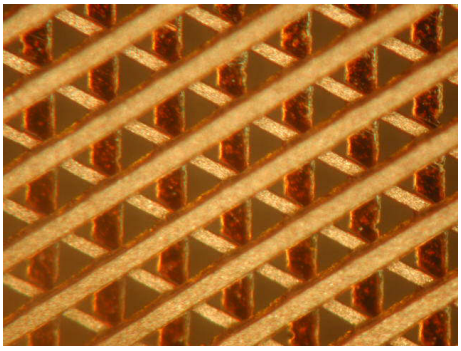

Figure 4.6: Closeup view of the 3D-FGLD microstructure made of patterned polyimide foils.

sandwich 100μm thick with the electrodes precisely aligned. The polyimide and excess glue are subsequently removed by chemical etching from the inter-electrode regions and then treated with a special cleaning procedure. A photograph of the finished 3D-FGLD foil is shown in figure 4.5 while a microscope image of its active area is shown in figure 4.6. The strips are spaced at a pitch of 150μm and their widths are 50μm, 30μm and 50μm thick on the TOP, MID, and BOT electrodes, respectively.

4.2.3 FGLD based on a uni-axis conductive mesh

An exciting new technology in the CERN workshop has been the micro-mesh material used for creating MPGD structures as in the example of the Micromegas in bulk. The fine-woven meshes open new geometric possibilities in MPGD design and we set out to build an FGLD based on a similar mesh to the one used for producing MicroMEGAS in bulk, but differing in that it has

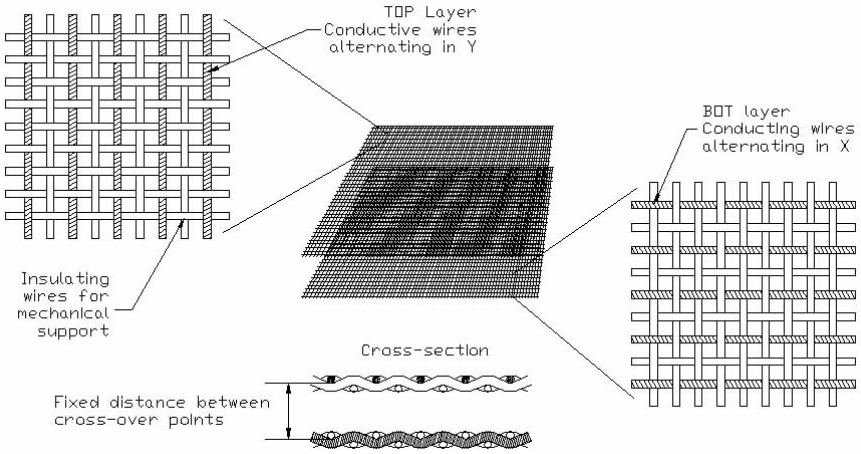

Figure 4.7: Schematic representation of the FGLD concept based on layers of a uni-axis conductive (UCM) mesh.

one axis of the tram made of metal and the other of insulating material. The so called *uni-axis conductive* mesh (UCM), was purchased from a standard manufacturer on our request having 20μm stainless steel in one tram and similar-sized polyester wires in another and a tram size of 200 lines per inch or 121μm pitch. A schematic representation of an FGLD based on such a mesh is shown in figure 4.7.

Laminating several UCM meshes into a sandwich with layers of solder-mask and then developing the solder mask to open the active area, we were able to produce 2D and 3D FGLD structures. Support for the mesh was provided by round pillars of mask having 300μm diameter and spaced at a few millimeters apart. Several 2D and 3D prototypes were made with various solder mask thickness, from 70μm to 200μm. Figure 4.8 shows a 3D-FGLD prototypes in which the three meshes are aligned at 90° with respect to one another. Electrical connection to the mesh layers was accomplished using silver epoxy. The active area of a 2D UCM-FGLD as seen through the microscope is shown in figure 4.9.

A difficulty in developing the polymer spacers when laminating multiple layers of mesh and mask was soon observed. A photograph of poorly formed spacers revealed upon dissection of a detector is shown in figure 4.10. The mesh has been rolled back to expose the underside of the spacers which are tapered due to poor development. The spacers are at intervals of 300μm from each other but have poorly defined height due to their rounded shape. The defect is the result of the finite penetration depth of the UV photons used to polymerize the solder mask during the image transfer step. Once the thickness of the solder mask is more than about 150μm, the photons have

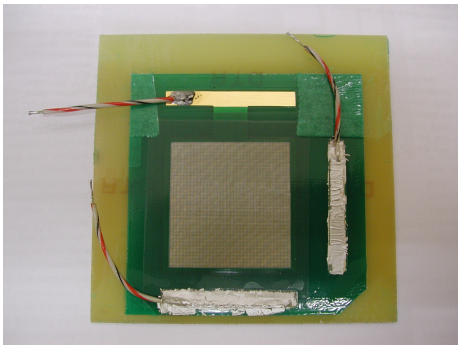

Figure 4.8: 3D UCM-FGLD prototype with active area of 3x3cm.

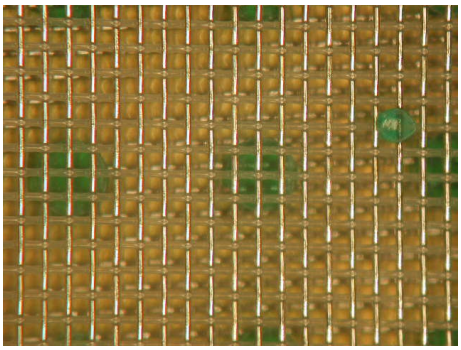

Figure 4.9: Closeup view of a 2D UCM-FGLD produced in the workshop. Each mesh has stainless steel wires of 20um diameter and the tram is 200 lines-per-inch (121um pitch). The insulating wires are polyester.

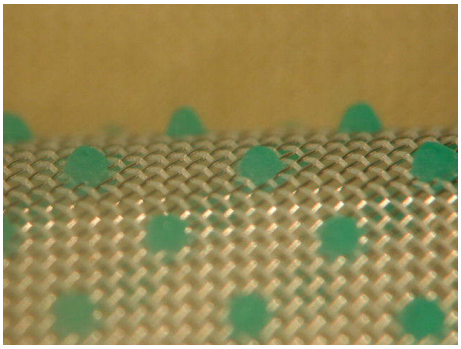

Figure 4.10: Poorly developed spacers in a uni-axis conductive mesh FGLD. The mesh has stainless steel wires of 20μm diameter and has 200 wires-per-inch.

attenuated enough that the pillars come out poorly developed. Increasing the number of meshes in the stack-up compounds the problem. It may be possible to improve on this problem by using thinner or more transparent photoimagable materials. Also of interest would be a finer woven mesh and wires of smaller diameter on a scale comparable to the meshes using in Micromegas in bulk. At the time, the manufacturer was not able to provide any uni-axis conductive mesh with conductive wires smaller than 20μm and development of 3D FGLD architectures using meshes has been paused until new materials are available.

4.2.4 Hybrid FGLD constructions

To shed some light on the performance of FGLDs based on uni-axis mesh material, we created a simplified version of the structure in which one mesh is replaced by strips on a rigid epoxy substrate. The structure, shown in 4.11 is more simple to produce than the uni-axis mesh FGLD in that fewer layers of solder-mask and only one mesh are laminated onto a prepared substrate with the BOT strips. This has the benefit of making the development process more reliable.

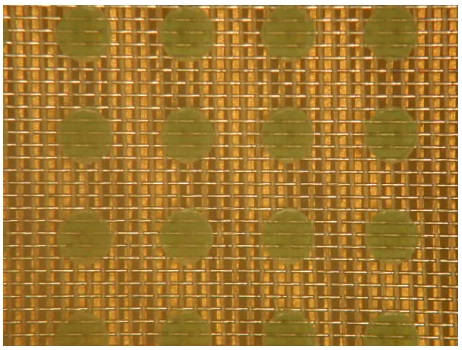

Figure 4.11: Closeup view of a 2D hybrid FGLD based on a uni-axis conductive mesh and strips on rigid substrate. The mesh has stainless steel wires of 20μm diameter and the tram is 200 lines-per-inch while the anode strips below are 75μm wide at 150μm pitch.

Chapter 5

Evaluating the FGLD

5.1 General setup for evaluation of proof-of-concept prototypes

FGLD prototypes produced using the various technologies described above were evaluated for performance while in operation in a gas drift chamber. Voltage was applied to each of the electrodes in the detector setup through $10M\Omega$ polarizing resistors connected to individual CAEN model 471A power supplies. Each electrode layer of the FGLD under test, grouped together in a proof-of-concept design, was read out through a decopling capacitor connected to a simple charge-sensitive preamplifier whose sensitivity was calibrated using an injection pulse of known charge. By measuring the pulse-heights of events produced in the detector from known X-ray sources, we were able to study the gain properties of the FGLD prototypes using different voltage configurations and gas mixtures. An example of a typical biasing schematic of the FGLD is shown in figure 5.1 along with the electronics chain employed for digitizing the signal and producing a pulse-height histogram of events in the detector. As shown in the schematic, the BOT layer was always made the anode (most positive voltage) of the detector setup and the TOP electrode voltage often set equal and opposite. In the 3D structure, the MID electrode is held at GND and in this way the symmetric voltage applied to the detector is stated simply as $\pm V$.

5.2 Gain calibration using radioactive sources: Fe55 and Cd109

5.2.1 3D in polyimide FGLD

Several 3D FGLD prototypes made from copper-clad polyimide foils were tested in a gas chamber containing an Argon CO_2 gas mixture. An ^{55}Fe source was used to create primary electrons in the gas volume and we used

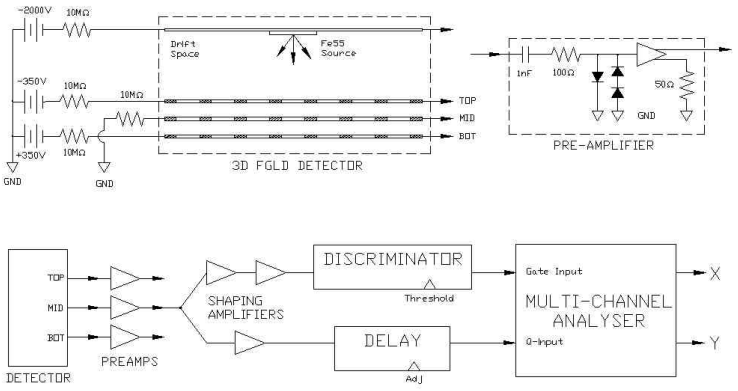

Figure 5.1: Biasing schematic of the 3D FGLD and typical readout electronics for digitizing the pulse-height information.

typically -1500V on the drift electrode held at 3mm from the FGLD detector to drift the primaries towards the detector. We applied symmetric voltage configurations to the detector itself while holding the MID electrode at ground. At voltages in the range of ±330V to ±360V, we observed pulses on the electrodes caused by the presence of the ^{55}Fe source held near the detector window. Figure 5.2 shows a sample pulse in the BOT electrode as seen on the scope. The signal has a rise-time of about 50ns which is likely due to the significant integration of the signal caused by the preamplifier. Pulses seen on the MID and TOP electrodes were always of opposite sign to those seen on the BOT. By digitizing the pulses of the electrodes and making a histogram of a large number of samples, we recorded numerous energy spectrums such as those shown in figures 5.3, 5.4, and 5.5, taken from the TOP, MID, and BOT electrodes, respectively. Using the position of the 5.9keV photo peak in the BOT spectrum along with the preamplifier response to a known injected charge, we were able to study the effective gain of each prototype detector as a function of the applied symmetric voltage. The gain curve for one of the better performing prototypes is shown in figure 5.6 for a gas mixture of Ar:CO_2(9%). We were able to reach gains of up to 5000 before inducing discharges at around ±400V.

Not all prototypes exhibited the same performance characteristics. The maximum effective gain achievable before working in a hazardous discharge regime was observed to depend strongly on the geometry of the 3D microstructure. Typically, both a better alignment of the mutual cross-over of strips between layers *and* a more uniform double-conical profile of the polyimide etching resulted in a higher achievable gain. In samples with lower gain, the 5.9keV photo peak was often lost in the noise of the pream-

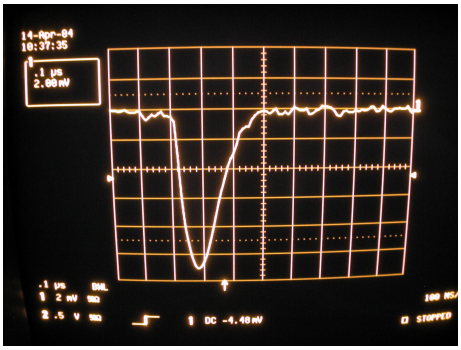

Figure 5.2: A sample pulse as seen on the scope from the BOT electrode of the 3D FGLD in polyimide under irradiation by an ^{55}Fe source.

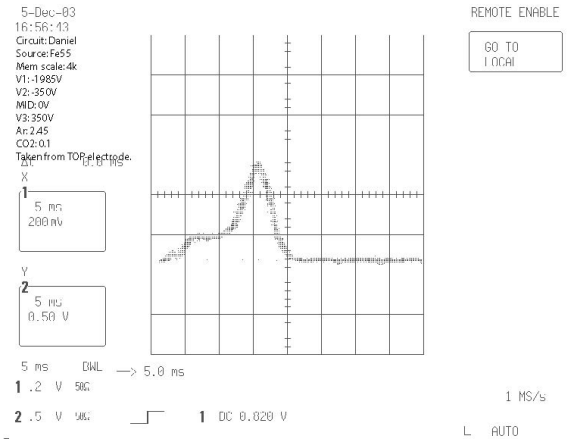

Figure 5.3: ^{55}Fe spectrum obtained from the TOP electrode of the 3D FGLD in polyimide.

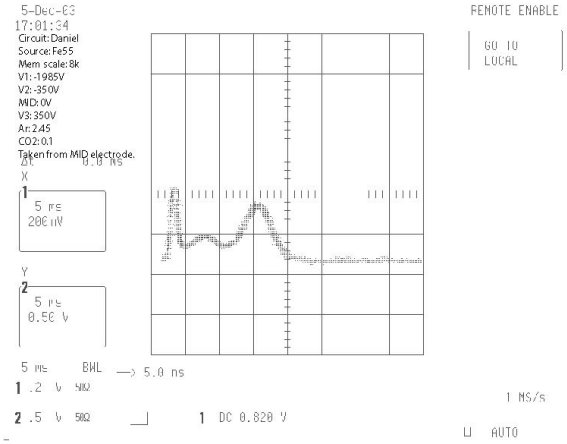

Figure 5.4: ^{55}Fe spectrum obtained from the MID electrode of the 3D FGLD in polyimide.

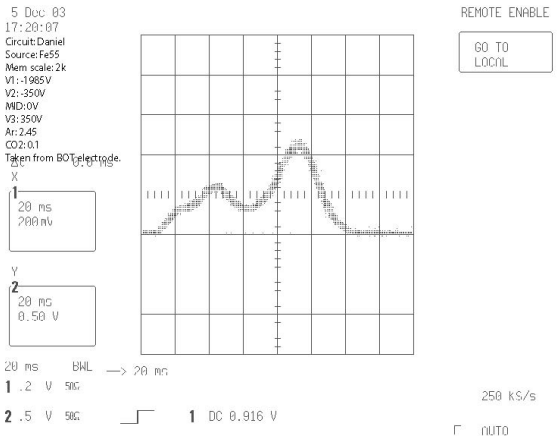

Figure 5.5: ^{55}Fe spectrum obtained from the BOT electrode of the 3D FGLD in polyimide.

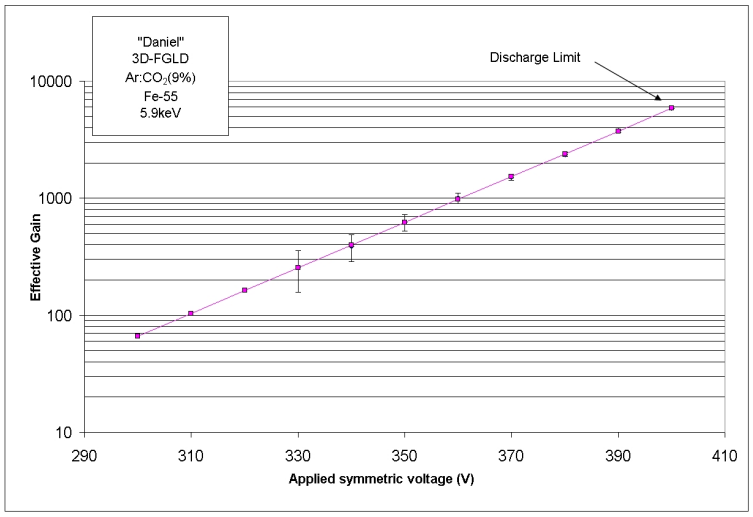

Figure 5.6: Gain calibration of a 3D-FGLD in polyimide under irradiation by 5.9keV X-rays from an ^{55}Fe source.

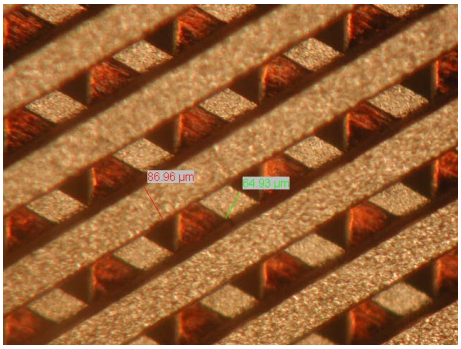

Figure 5.7: Microscope view of a 3D FGLD with 200μm-pitched electrodes.

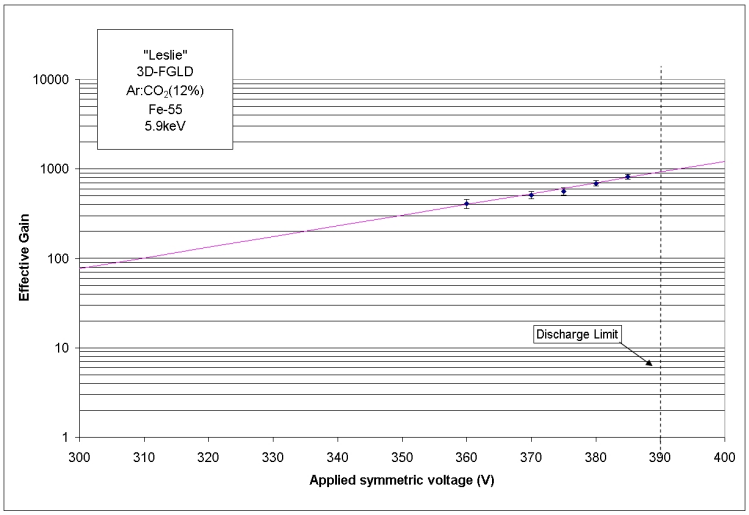

Figure 5.8: Gain curve of a 3D FGLD in polyimide with 200μm-pitched electrodes.

plifier and only visible at larger voltages in the limit of discharges. To compensate for the low signal-to-noise and to be confident of the measurement of the X-ray photo peak, we used the larger 22keV energy peak from a ^{109}Cd source to make our calibration. In addition to prototypes with 150μm-pitched electrodes, we created one having 300μm pitch and one having 200μm pitch. Figure 5.7 shows microscope view of the active area of the 200μm detector. The 200μmm detector was calibrated with the ^{109}Cd source and the gain curve is shown in figure 5.8. The maximum achievable gain was only 800 though the discharge limit was $\pm$390V, similar to the 150μm prototypes. The energy resolution was quite low, around 40% at 5.9keV. With the 300μm detector we were unable to resolve pulses from either of our radioactive sources. A summary of the findings for several 3D FGLD prototypes in polyimide is given in table 5.1.

ID	Pitch	Max Gain	Energy Res.	Discharge Limit	Alignment
Daniel	150μm	5000	28%	$\pm$390V	Excellent
Edgar	150μm	3500	35%	$\pm$375V	Excellent
Franc	150μm	1200	40%	$\pm$360V	Acceptable
Herbert	150μm	1000	50%	$\pm$385V	Poor
Ivan	150μm	1000	50%	$\pm$360V	Poor
Jul	150μm	2500	35%	$\pm$410V	Excellent
Kim	300μm	N/A	N/A	$\pm$390V	Excellent
Leslie	200μm	800	40%	$\pm$390V	Acceptable
Mark	150μm	1200	40%	$\pm$365V	Acceptable

Table 5.1: Summary of performance of 3D-FGLD prototypes built with polyimide technology. The results are for Ar:CO_2(15%) gas mixture.

The overall gain performance of the prototypes, including their stability of operation, was generally worse in detectors having misaligned geometries or poorly-etched polyimide though a number of other factors are thought to also play a role, including the profile of the copper strip electrodes and their surface qualities. Because the fabrication method employed for building the 3D microstructure is complex, there arise a countless number of parameters which can be modified in the production procedure which are often very difficult to control precisely. For this reason, a detailed and systematic study of the gain characteristics as a function of the various production variables is still missing and could explain the rather large differences in performance observed in the prototypes. Furthermore, even detectors having the best alignment in the center of the active area were slightly unaligned near the edges. This is probably the result of stretching of the polyimide during the gluing step which is done under pressure in a press machine. Some efforts have been made to reduce the pressure needed in the gluing step while maintaining a good adhesion. This improves the overall alignment but because of the number of other free variables, results are not yet conclusive as to whether alignment is the primary cause of gain variation and/or low energy resolution in the 3D-FGLD.

5.2.2 Uni-axis conductive mesh FGLD

We conducted similar gain calibrations on the FGLD prototypes based on 2 and 3 layers of uni-axis-conductive mesh. Our findings indicated that the gain was much lower than in the polyimide-based prototypes. Figures 5.9 and 5.10 show the gain characteristics obtained with ^{109}Cd in two 2D UCM-FGLD prototypes where the spacing between meshes is 150μm and 200μm, respectively. We were able to obtain stable gains of only 350 in the 150μm structure and 500 in the 200μmm structure.

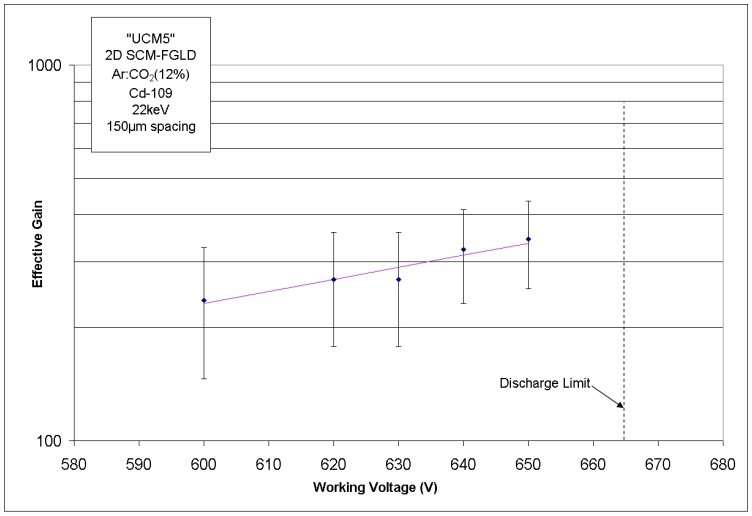

Figure 5.9: Gain calibration curve at 5.9keV for a 2D uni-axis conductive FGLD having 150μm separation between meshes.

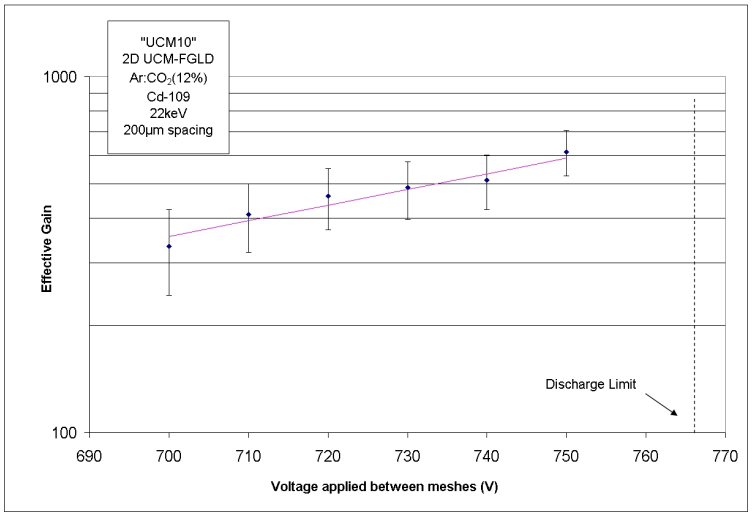

Figure 5.10: Gain calibration curve at 5.9keV for a 2D uni-axis conductive FGLD having 200μm separation between meshes.

5.3 Current measurements using Cu X-ray tube

5.3.1 Setup

To more accurately study the performance of the 3D-FGLD prototypes, we employed an X-ray tube which uses a copper anode to produce X-rays peaked at 8.9keV. The tube is powered by a 15kV generator which allows the user to vary the current up to 4.0mA. FGLD's with active area 3cmx3cm were mounted in a gas chamber containing Ar:CO_2 (30%) and a drift electrode larger than the active area was spaced at a distance of 4.5mm from the detector's TOP electrode. The electrodes, including drift, were powered by separate CAEN 471A model supplies, and the BOT electrode, held at GND through a $1M\Omega$ resistor, was readout with an Ortek preamplifier. The CAEN modules provided the current measurement for the biased electrodes, while the BOT electrode current was readout using a Keitley voltage meter across the $1M\Omega$ resistor. Studies were made of the detector's characteristics under irradiation from the X-ray tube. Two collimators were used having 1mm and 3mm diameters.

5.3.2 Rate calibration

In order to calculate the gain in the detector from the measured BOT electrode photo-current, we must know the rate of X-rays which are converting in the gas volume as a function of the generator current. By counting the pulses produced by a discriminator with threshold set above the noise and varying the current to the X-ray tube, we obtain the curve shown in red in figure 5.11 for a 1mm collimator and 3mm drift gap. The actual rate, however, is extrapolated from the initial linear region of the curve since the electronic dead time quickly saturates the measurement at X-ray currents above 0.100mA. Different drift gaps were calibrated individually.

5.3.3 3D-FGLD in polyimide

We began measurements with a sample of the 3D-FGLD in polyimide having 150μm-pitched electrodes and mounted in a chamber with 4.5mm drift. Using a voltage of -800V and -400V on the TOP and MID electrodes, we recorded the photo-currents while increasing the current to the X-ray tube generator. Figure 5.12 shows the currents on the drift, TOP, MID, and BOT electrodes up to X-ray currents of 1mA. The response of the detectors to the increasing flux of photons is perfectly linear indicating a stable gain operation and a linear behavior of the flux in response to the generator current. As required, the sum of the charge equals zero at all currents. It is also interesting to note the distribution of the positive charge reabsorbed in the detector electrodes. Taking the negative BOT current being 100% of the charge, the TOP electrode represents 80% and the MID 10% of the positive

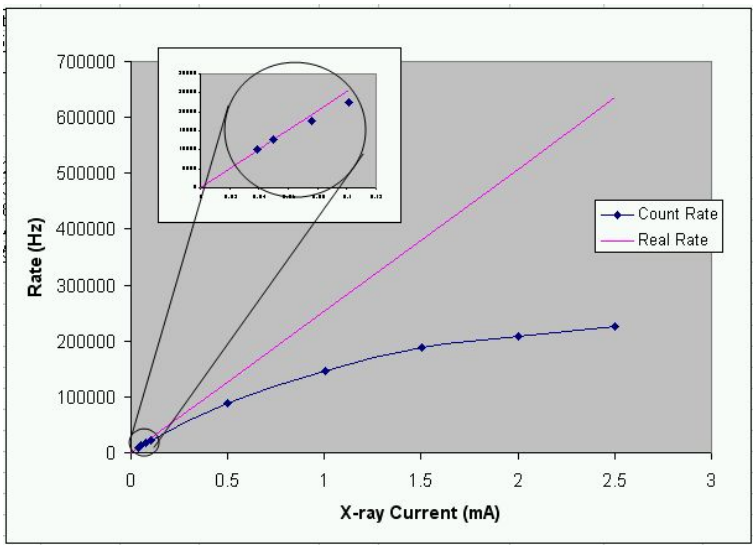

Figure 5.11: Measured count rate and extrapolated count rate in the 3D-FGLD as a function of X-ray generator current.

charge while 10% leaves the detector and is absorbed on the drift electrode. The sharing of the positive charge indicates the expected values of the useful gain for the various electrodes, an important consideration for electronics design in a fully-equipped FGLD with active multi-channel electronics.

The 3D-FGLD in polyimide also showed excellent energy resolution at a moderate rate of the X-ray tube as shown in figure 5.13. The energy resolution is 24.3% FWHM and the X-ray tube, collimated to 1mm, gives a rate of 4kHz/mm2.

To study the effect of ion feedback and to more deeply understand the nature of the avalanche mechanism in the 3D-FGLD, we measured the photocurrents on all electrodes keeping the detector fixed at ±400V and varying the voltage applied to the drift. Figure 5.14 shows the currents plotted as a function of the applied electric field in the 4.5mm drift region. The spike in the curve at -1600V/cm is the moment when the drift velocity of the primary ionization exceeds the threshold for recombination. Fully efficient transport of the charge is reached at a drift field of 2000V/cm where the detector is attracting the charge, amplifying it, and collecting it. Above this value, the positive current absorbed on the drift electrode increases linearly, indicating the behavior of the drift field to extract positive ions produced in the avalanche amplification within the FGLD foil. Interesting is the nearly constant value of the MID current in the operating region regardless of the value of the drift voltage. This could be an indication for a dual stage amplification mechanism within the 3D electrode structure where the ions collected on the MID electrode are a portion of those created in an avalanche

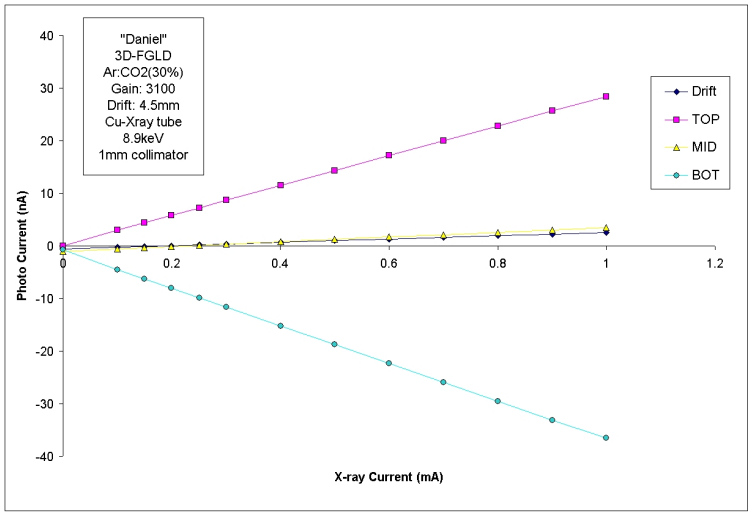

Figure 5.12: Photo currents induced in the electrodes of a 3D-FGLD in polyimide. The voltage configuration on the detector is symmetric (±400V) and the gain is 3000.

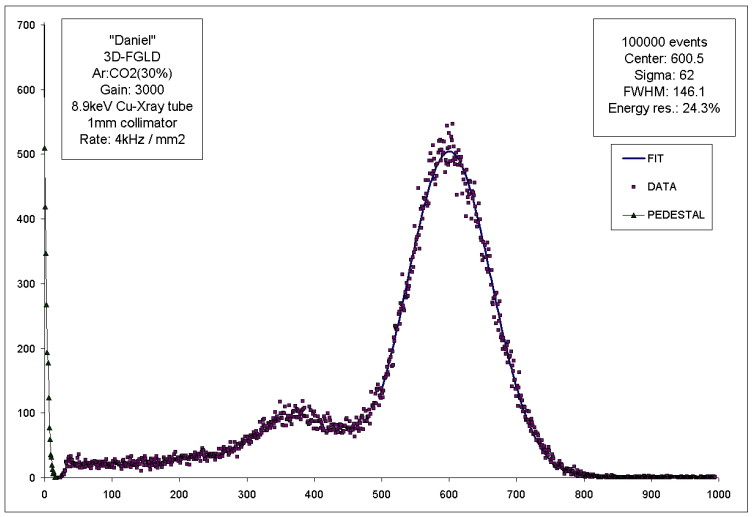

Figure 5.13: Pulse height spectrum of Cu 8.9keV X-rays taken from the BOT electrode of a 3D-FGLD in polyimide. The X-ray tube is collimated to 1mm diameter and the energy resolution is 24.3%.

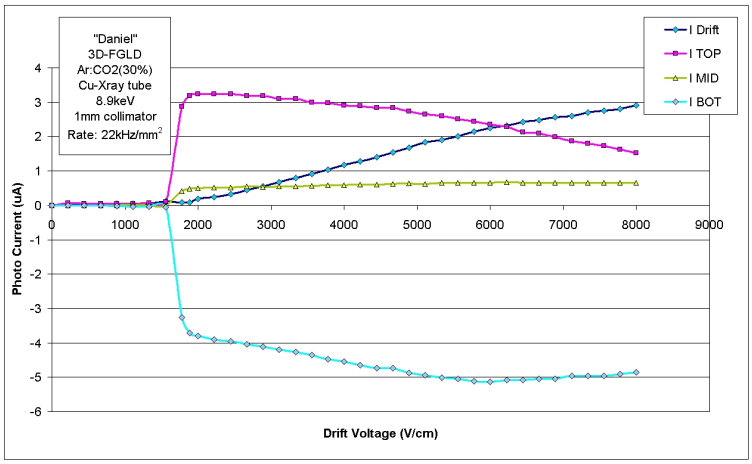

Figure 5.14: Electrode photo-currents in the 3D-FGLD in polyimide as a function of the drift field. The voltage configuration on the detector is symmetric (±400V) and the gain is 3000.

between the MID and BOT layers. The fraction of the ions collected on the MID layer is probably determined by the ratio of the MID-BOT field to the TOP-MID field which was held constant during this measurement though further study is needed to confirm this. For subsequent measurements we applied a drift voltage of -1000V, corresponding to a field of 2200V/cm, where the gain suffers the least variation and the ion feedback is low.

We performed a detailed gain calibration using non-symmetric voltage configurations. The gain of the detector was calculated from the current on the BOT electrode and in figure 5.15 we plot the result upon making scans of the voltage between the TOP and MID electrodes at various voltages between MID and BOT.

The gain response of the detector smoothly follows the applied voltage in an intuitive way. Somewhat intriguing, is the fact that regardless of the configuration applied, the discharge limit remains solidly fixed at a gain of just above 5000. This may be due to an effect related to X-rays penetrating the copper of the TOP layer of the detector followed by photo-electron emission. If the electron is emitted near the edges of a strip, in a region of high-electric field gradient, it will follow a path of higher overall acceleration on its way to the anode and if the rather limit is surpassed, the avalanche becomes a streamer and the detector discharges. An effect like this should depend on the rate of X-rays incident on the detector's upper copper layers and indeed it was noted that closing the shutter on the X-ray tube allowed us to increase the voltages to higher levels with less discharges.

The 3D polyimide prototype also performed well under high-rate irradiation. Increasing the generator current to up to 4mA and using the 1mm

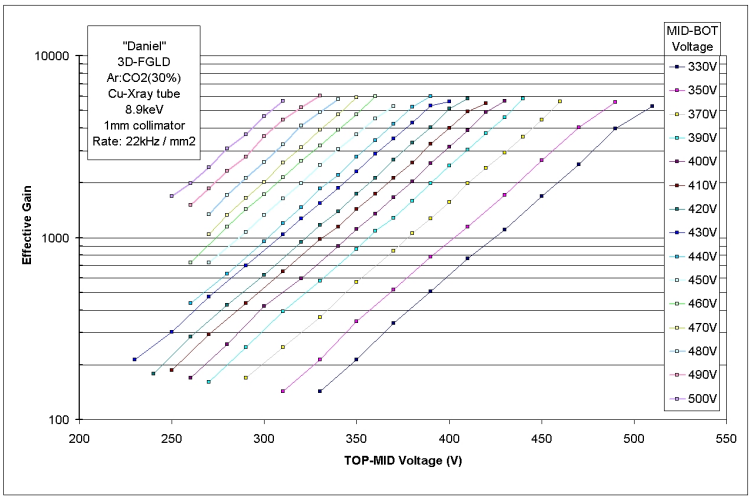

Figure 5.15: Gain curves of the 3D-FGLD in polyimide shown for different voltage configurations applied between the TOP, MID, and BOT electrodes. The BOT electrode is the anode in all configurations shown.

diameter collimator, we were able to achieve rates of up to 1Mhz/mm^2. Figure 5.16 shows the photo-currents on the electrodes of the 3D-FGLD at a gain of 3100V as a function of the rate. The response on all three electrodes is entirely linear up to the maximum rate of 1MHz/mm^2. No degradation in performance was observed using the 1mm diameter collimator over the full range of the generator current.

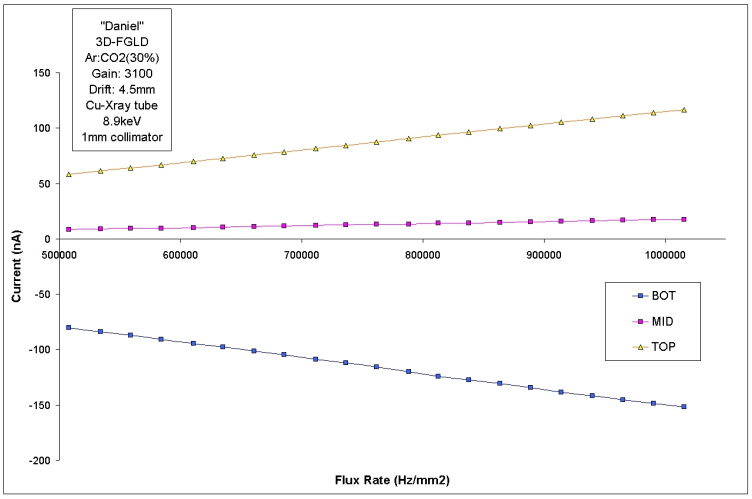

Figure 5.16: Photocurrents on the 3D FGLD in polyimide electrodes from 1mm collimated Cu X-rays at rates up to 1MHz/mm^2.

Chapter 6

3D-FGLD readout with portable DP-GP5 electronics

6.1 The DP-GP5 front-end

In order to study the ability of the FGLD to record the position information of ionizing events in the gas volume and to produce useful images relevant for imaging applications, we set out, in parallel to the fundamental detector research, to develop a readout electronics data aquisition (DAQ) system based on a self-triggering multi-channel front-end IC. We selected a commercial multi-channel charge preamplifier chip: the IDEAS's VATAGP5 [24] as the backbone of the front-end. Each of the 128 channels has two bi-polar shaping preamplifiers: a fast 40ns shaper with comparator for trigger and a slower 250ns shaper for precision amplitude measurement. A DAC adjustment is provided on each channel for custom threshold settings. The analogue pulse height can be read out in serial, sparse and sparse with neighbors readout modes.

In order to protect the chip's inputs from discharges we adapted a multi-channel diode protection IC originally developed for use as an element in a front-end readout for the triple-GEM detectors of the TOTEM experiment [25]. Our front-end solution is a combination of the VATAGP5 and diode protection chips, which we call the DP-GP5. Figure 6.1 is a close-up photo of the DP and GP5 chips mounted together on a custom PCB hybrid. Analogue to digital conversion and biasing was provided with a special DAQ board capable of decoupling the output and control signals from voltages up to $\pm$600V. This was needed for operating the FGLD which necessarily requires the readout electrodes to be at high voltage during operation. A portable Altera-based DAQ having a QuickUSB module [26] for PC communication was used for data handling and chip programming. Data taking and offline data analysis was made using Labview.

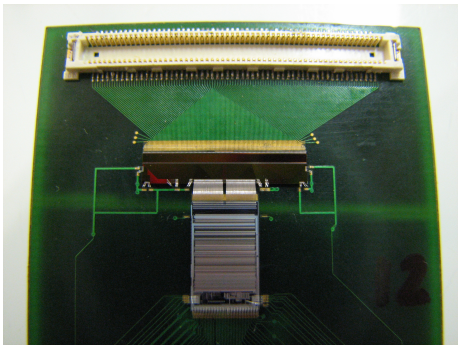

Figure 6.1: The DP-GP5 front-end electronics mounted on a custom hybrid with board-to-board connector for link between the detector and electronics.

6.2 Noise and lowest threshold for trigger

The DP-GP5 electronics was first calibrated without connection to the detector by charge injection. We used three capacitors, 1.8pF, and two of 18pF, connected in series to different channels of the electronics and driven by a pulse generator. A plot of the average ADC response for several thousand events in one of the hybrids is shown in figure 6.2 as a function of the injected charge. The response of the GP5 with diode protection chip is linear within 15% up to 1pC input charge and within 35% at its maximum dynamic range, 3pC. The noise on each connected channel was observed to increase with the value of the capacitor. Converted into units of charge, we can state roughly that the DP-GP5, when not connected to the detector, has an analogue noise of 0.8fC + 0.25fC/pF or 5500e +1500e/pF.

In order to characterize the lowest threshold, we programmed the chip to trigger on *one* of the connected channels or on *all* channels and fixed the threshold just above the noise in each case. A plot of the trigger rate as a function of the injected charge is shown in figure 6.3. Maximum efficiency is reached around 6fC for the single channel trigger with a 1.8pF injection capacitor, 20fC for the 18pF capacitor on single channel and 40fC when all channels are programmed for trigger. The lowest threshold for single trigger matches closely the given parameter in the GP5 datasheet of 3.5 to 6fC. On all channels trigger however, the lowest threshold is much higher due to the pedestal offset which makes some channels trigger before others when using a global threshold. The GP5's internal DAC adjustment - programmable for each channel - is designed to compensate for this effect but at the time of writing has not been used in our studies.

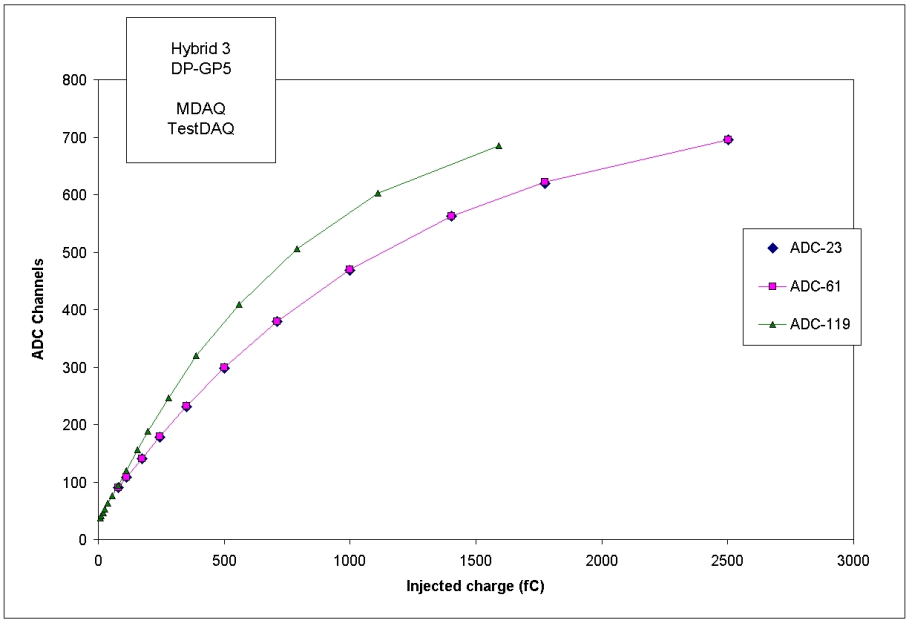

Figure 6.2: The digitized response of injected charge in the DP-GP5 readout system. The GP5 has a high-dynamic range up to 3pC input charge with 15% linearity in the range of 0 to 1pC.

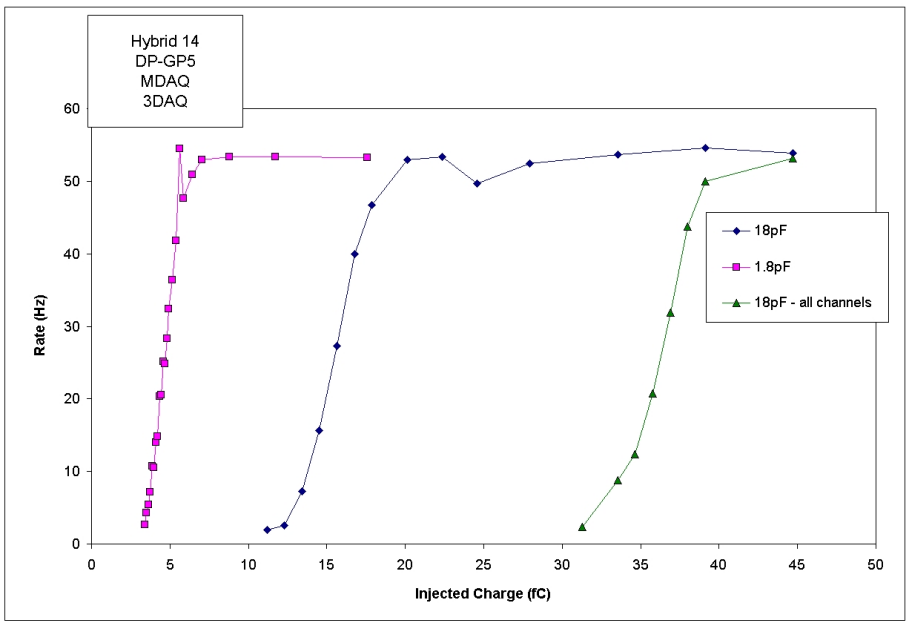

Figure 6.3: Lowest threshold estimation for single channel 1.8pF, single channel 18pF, and all channels injection.

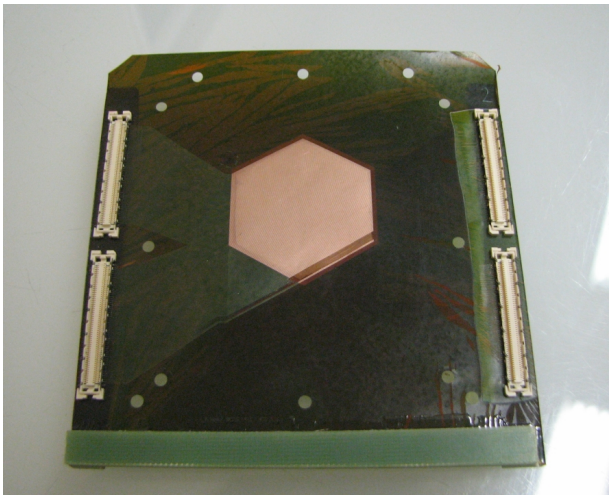

Figure 6.4: A 3D-FGLD designed for readout with the DP-GP5 front-end electronics.

6.3 Setup of electronics and detector

The electronics was used for studies of a newly designed version of the 3D-FGLD in polyimide having an active area of 3x3cm and strips of standard geometry of 150μm pitch. We made the connection between detector and electronics using board-to-board connectors and a picture of a 3D-FGLD for this purpose is shown in figure 6.4. The detector was mounted in a gas chamber and the mechanical setup of the detector with front-end hybrids and DAQ boards is shown in figure 6.5. Two hybrids are needed for each layer of the detector and only the TOP and BOT layers are equipped. We connected the MID layer to ground for our studies since previous results have shown that ratio of charge collected on the MID layer is only 10% of the BOT layer. The typical operating gain is between 1000 and 5000, corresponding to a collected charge of 35 to 175fC for 5.9keV photons if we look to the BOT electrode. As such, obtaining the signal in the MID layer, which should be around 17.5fC at best, would require us to operate at unsafe and unstable voltages in the limit of discharging. The task of reading out all three axes of the FGLD is left for future developments.

6.4 Energy resolution and linearity

We collected ^{55}Fe and ^{109}Cd events from the TOP and BOT electrodes in a 3D-FGLD using our DP-GP5 electronics. We selected a single channel in the BOT electrode and programmed it to provide trigger for the readout of all 256 channels of both TOP and BOT layers. The trigger threshold was positioned to a level just above the noise and data runs of 10000 to

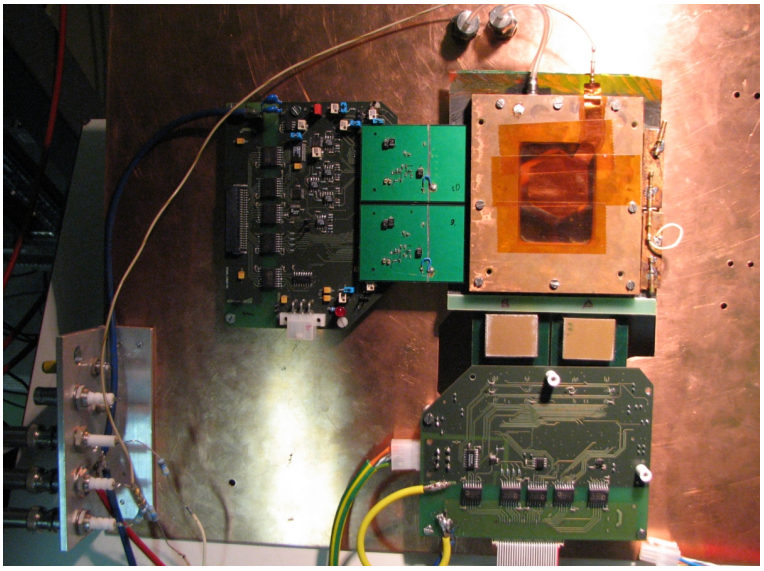

Figure 6.5: Gas chamber for testing the 3D FGLD with readout electronics.

30000 samples were recorded and analyzed offline using a software which substracts pedestal and executes a complex common-mode (CM) rejection algorhythm to filter the CM noise and sum the resultant charge shared over multiple channels. Figure 6.6 was made at a working gain of ±360V in Argon:(15%)CO_2 and shows the ^{55}Fe and ^{109}Cd pulse-height spectrums created in the analysis software. The photo peaks at 22keV, 5.9keV, and the escape peak at 3keV are spaced apart horizontally in proportion to their energy as expected if the electronics is operating in its linear charge-sensitive regime. Using the gain of the front-end electronics, calibrated previously through charge injection, and the position of the various photo peaks in the spectrum, we are able to calculate the effective gain of the detector. Figure 6.7 shows the position of the photo peaks as a function of their energy for three different detector gains. The response is linear with respect to the charge collected on the detector and the gain performance is consistent with previous 3D-FGLD results.

6.5 2-axis measurement and charge sharing characteristics

While setting the trigger on *only* two channels, one on the BOT layer and one on the TOP, we recorded the data from the TOP and BOT under irradiation by ^{55}Fe. In figure 6.8 we show a screenshot of the analysis software showing the spectrums obtained on the TOP and BOT electrodes at a gain of 5000. The ratio of the TOP peak's position to the BOT's is 74%, in accordance

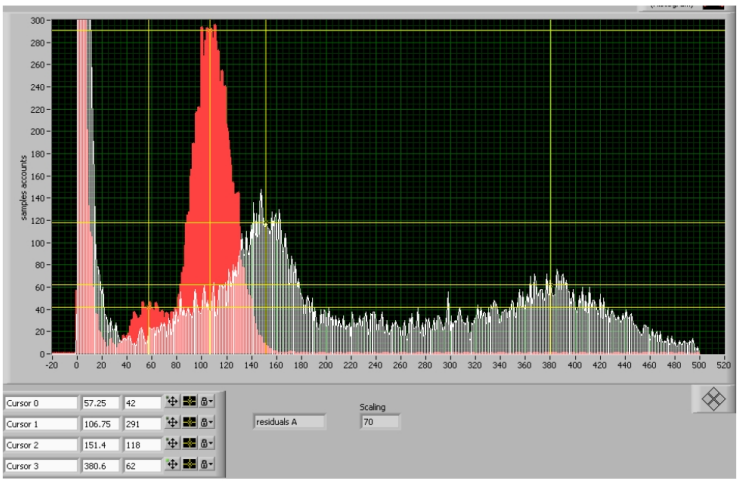

Figure 6.6: Energy spectrums of ^{55}Fe and ^{109}Cd sources taken from the BOT electrode at a gain of 5000 using the DP-GP5 readout electronics. The energy resolution is 42% FWHM at 5.9keV.

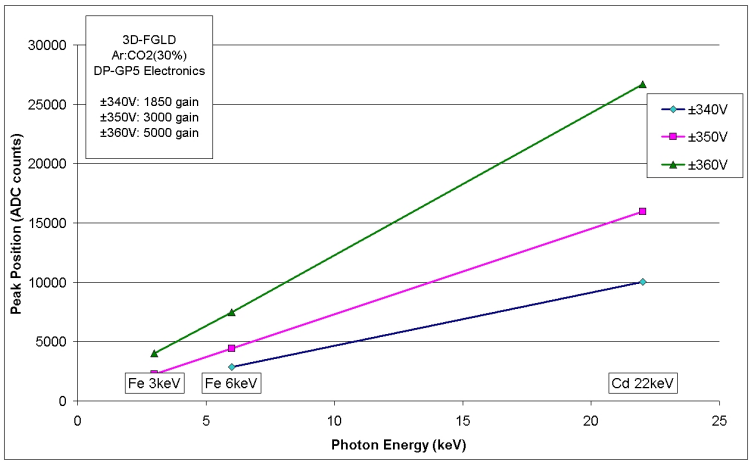

Figure 6.7: Linearity of position of photo peaks from ^{55}Fe and ^{109}Cd at three different gains in the 3D-FGLD readout with DP-GP5 electronics.

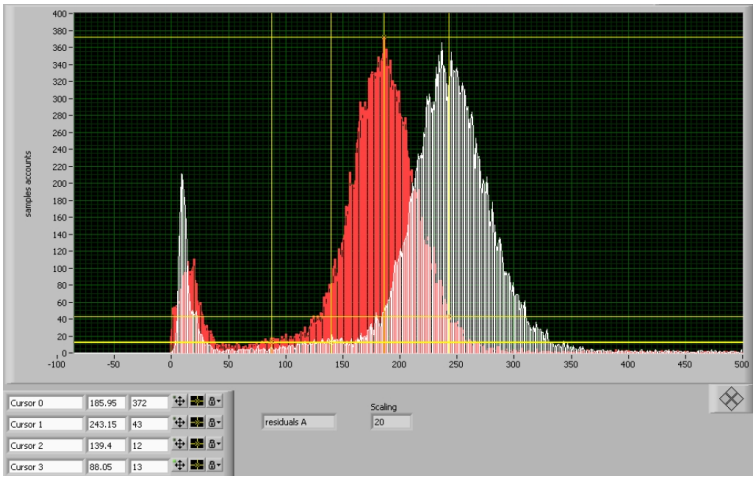

Figure 6.8: Charge sharing of ^{55}Fe events in TOP (red) and BOT (white) electrodes at a gain of 5000.

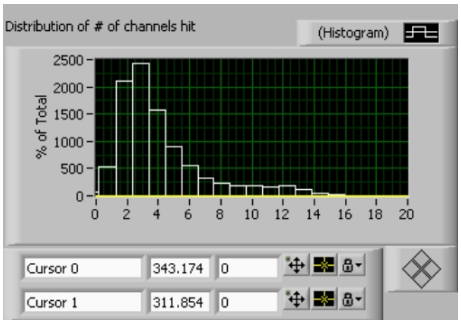

Figure 6.9: Charge cluster distribution (number of strips hit per event) of ^{55}Fe events in the BOT electrode at a gain of 5000.

with the sharing of photo-currents in the X-ray detector measurements. The energy resolution of the BOT electrode spectrum is 30% FWHM and we see noise in both spectrums arising when the event triggers only one strip. Analyzing the data offline, we were able to find the number of strips involved in charge collection on an event by event basis and the distribution from the BOT electrode data is shown in figure 6.9. The charge is shared predominantly on 3 channels, corresponding to cluster sizes in the range of 450μm.

In order to test the imaging performance of the detector and electronics, we collimated the ^{55}Fe source to 1mm diameter as in the schematic drawing shown in figure 6.10. Because the source has a finite size and was positioned not far from the detector to obtain a better rate, the actual X-ray beam incident on the detector volume varies from about 3 to 4mm. We produced the intensity reconstruction shown in figure 6.11 by taking the maximum

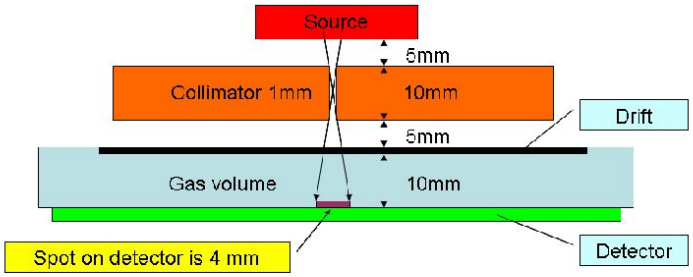

Figure 6.10: Schematic drawing showing the geometry of the ^{55}Fe source and 1mm collimator used for making an image reconstruction.

strip value to be the center of each charge cluster. The image in the reconstruction software is elliptical though the collimator is cylindrical. The deformation is an artifact of the projection of the 60-degree-rotated configuration of the 3D-FGLD design and can be easily removed in the offline analysis. The distribution spans about 20 strips or 3mm at its widest in close agreement to the beam size expected from the source and collimator geometry.

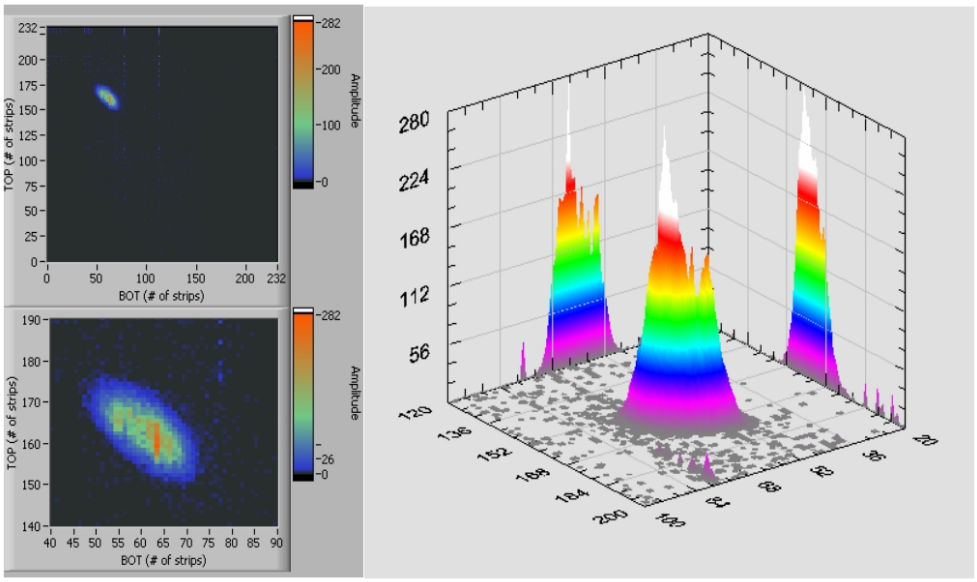

Figure 6.11: Reconstruction of a collimated ^{55}Fe source using the DP-GP5 electronics.

Chapter 7

Discussion and Conclusion

The FGLD has been produced using a variety of production techniques and its performance and characteristics have been seen to depend quite strongly on the geometry of the electrodes. Efforts to produce a 2D FGLD using epoxy resin technology and the 3D FGLD structure using a uni-axis conductive mesh were stopped for production difficulties. The 3D in polyimide technology shows the most promise, and although the fabrication technique is quite delicate and challenging, much progress has been made to improve the process and detectors can now be built reliably in sizes having 3x3cm^2 active area. Stable gains of up to 3000 in argon-CO_2 gas mixtures, far from the regime of discharges, have been achieved with many different detectors and gains of 5000 should be possible with some improvements to the production.

Tests with a high flux of X-rays collimated to 1mm^2 were admirable. Though we didn't irradiate the detector over the entire active area, the 3D prototype showed a perfectly stable performance up to 1MHz/mm^2 the limit of the X-ray tube. The 3D structure could be used in high-rate tracking applications where the third axis of readout is needed for resolving ambiguities from coincidental events. Non-symmetric biasing of the detector electrodes could be one solution for overcoming the low signal of the MID layer, however, in many applications, including X-ray imaging where the photon energy is higher, this may not be an issue.

The energy resolution in the detector is moderate, typically around 40% when irradiating the entire active area which improves to about 30% when the source is collimated or when single channels are used to trigger readout. This is likely an artifact of the alignment of the cross-over regions of the strips in the three layers which varies slightly from one side of the active area to the other. The artifact arises during the pressing step of production in which the MID layer, encapsulated in the lamination, is stretched along with its polyimide support under the pressure. Some ideas exist to improve this, but alignment is one concern for 3D-FGLD operation in light of the

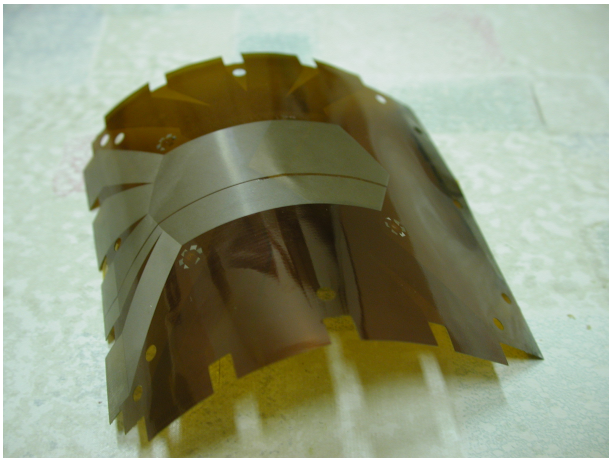

Figure 7.1: The flexible 3D-FGLD foil based on polyimide technology only 100μ thick.

poor results obtained with misaligned detectors.

A novel aspect that has been developed alongside the FGLD is a portable readout electronics based on the DP-GP5 front-end which can be connected to a computer using USB. After extensive studies with the FGLD, often at the detector's limit before breakdown, the DP-GP5 has proven resilient to numerous discharges and could therefore be used as a readout solution for any gas detector. Because it is self-triggering and has a variety of analogue and digital readout modes, it can be useful for a wide variety of applications in medical imaging and industry.

The FGLD is interesting for the elegance and simplicity of its design. As both the amplifying structure and the readout, it can be used as the sole element in a Micro-pattern Gas Detector assembly where a moderate gain and energy resolution is required. The compact structure provides a fast rising signal due to rapid collection of the ions produced in the avalanches inside the detector. Like the GEM, the FGLD is flexible and cylindrical detector configurations, employing the FGLD and/or GEM detectors, would be an interesting future development (see figure 7.1). At the time of writing efforts are on going to build the 3D FGLD structure with a larger active area, 10x10cm^2, though the strong performance dependence upon seemingly invisible production differences remains somewhat of a mystery. Further production studies, which could include simulation, are probably required if we want to optimize the detector's performance or tailor it to a specific application.

Bibliography

[1] http://physics.nist.gov/PhysRefData/contents.html

[2] F. Sauli, *Principles of operation of multiwire proportional and drift chambers*, CERN Geneva, CERN Academic Training Lectures, 81, 1977

[3] P. Rice-Evans, *Spark, Streamer, Proportional and Drift Chambers*, The Richelieu Press, London, 1974

[4] G. Charpak et al., *The use of multiwire proportional counters to select and localize charged particles*, Nucl. Instrum. Methods 62, 1968, pp 262

[5] A. Oed, *Position-sensitive detector with microstrip anode for electron multiplication with gases*, Nucl. Instrum. Methods A 263, 1988, pp 351

[6] Y. Giomataris, Ph. Rebourgeard, J.P. Robert, and G. Charpak, *MICROMEGAS: a high-granularity position-sensitive gaseous detector for high particle-flux environments*, Nucl. Instrum. Methods A 376, 1996, pp 29-35

[7] F. Sauli, *GEM: A new concept for electron amplification in gas detectors*, Nucl. Instrum. Methods A 386, 1997, pp 531-534

[8] A Bressan. M. Hoch, P. Pagano, L. Ropelewski, F. Sauli, S. Biagi, A. Buzulutskov, M. Gruwe, G. De Lentdecker, D. Moermann, and A. Sharma, *High rate behavior and discharge limits in micro-pattern detectors* Nucl. Instrum. Methods A 424, 1999, pp 321-342

[9] V. Peskov, P. Fonte, M. Danielsson, C. Iacobaeus, J. Ostling, M. Wallmark, *Fundamentals of gas micropattern detectors* arXiv:physics/0106016v1, 2001

[10] R.K. Carnegie, M.S. Dixit, J. Dubeau, D. Karlen, J.-P. Martin, H. Mes and K. Sachs, emphResolution studies of cosmic-ray tracks in a TPC with GEM readout Nucl. Instrum. Methods A 538, 2005, pp 372383

[11] F. Sauli, L. Ropelewski, and P. Everaerts, *Ion feedback suppression in time projection chambers* Nucl. Instrum. Methods A 560, 2006, pp 269-277

[12] De Oliveira, R., *Multi Chip Module Laminated-MCML* Patent App. No. FR02/04305

[13] S. Bachmann, A. Bressan, L. Ropelewski, F. Sauli, A. Sharma, and D. Mormann, *Charge amplification and transfer processes in the gas electron multiplier* Nucl. Instrum. Methods A 438, 1999, pp 376-408

[14] C. Shalem, R. Chechik, A. Breskin, and K. Michaeli, *Advances in Thick GEM-like gaseous electron multipliersPart I: atmospheric pressure operation* Nucl. Instrum. Methods A 558 (2006) 475489

[15] R. Oliveira, V. Peskov, F. Pietropaolo, and P. Picchi, *First tests of thick GEMs with electrodes made of a resistive kapton* Nucl. Instrum. Methods A 576, 2007, pp 362366

[16] M. Inuzuka, H. Hamagaki, K. Ozawa, T. Tamagawa, and T. Isobe, *Gas electron multiplier produced with the plasma etching method* Nucl. Instrum. Methods A 525, 2004, pp 529534

[17] S. Uno, M. Sekimoto, T. Murakami, N. Ujiie, T. Uchida, H. Kadomatsu, A. Sugiyama, S. Nakagawa, E. Nakano, *Performance study of new thicker GEM* Nucl. Instrum. Methods A 581, 2007, pp 271273

[18] F. Simon, B. Azmoun, U. Becker, L. Burns, D. Crary, K. Kearney, G. Keeler, R. Majka, K. Paton, G. Saini, N. Smirnov, B. Surrow, and C. Woody, *Development of Tracking Detectors With Industrially Produced GEM Foils* IEEE Transactions on Nuclear Science, Vol. 54, No. 6, December 2007, pp 2646-2652

[19] B. Ketzer, M. C. Altunbas, K. Dehmelt, J. Ehlers, J. Friedrich, B. Grube, S. Kappler, I. Konorov, S. Paul, A. Placci, L. Ropelewski, F. Sauli, L. Schmitt, and F. Simon, *Triple GEM Tracking Detectors for COMPASS* IEEE Transactions on Nuclear Science, Vol. 49, No. 5, October 2002, pp 2403-2410

[20] M. C. Altunbas, M. Capeans, K. Dehmelt, J. Ehlers, J. Friedrich, I. Konorov, A, Gandi, S. Kappler, B. Ketzer, R. de Oliveira, S. Paul, A. Placci, L. Ropelewski, F. Sauli, F. Simon, and M. van Stenis, *Triple GEM Tracking Detectors for COMPASS* IEEE Transactions on Nuclear Science, Vol 49, No 5, October 2002, pp 2403-2410

[21] P. Abbon, S. Andriamonje, S. Aune, T. Dafni, M. Davenport, E. Delagnes, R. de Oliveira, G. Fanourakis, E. Ferrer Ribas, J. Franz, T. Geralis, M. Gros, Y. Giomataris, I. G. Irastorza, K. Kousouris, J. Morales, T. Papaevangelou, J. Ruz, K. Zachariadou, and K. Zioutas, *A new Micromegas line for the CAST experiment* Nucl. Instrum. Methods A 581, 2007, pp 217-220

[22] I. Giomataris, R. de Oliveira, S. Andriamonje, S. Aune, G. Charpak, P. Colas, A. Giganon, Ph. Rebourgeard, and P. Salin, *Micromegas in a bulk* Nucl. Instrum. Methods A 560, 2006, pp 405-408

[23] J. Bouchez, D.R. Burke, Ch. Cavat, P. Colas, X. De La Broise, A. Delbart, A. Giganon, I. Giomataris, P. Graffin, J.-Ph. Mols, F. Pierre, J.-L. Ritou, A. Sarrat, E. Virique, M. Zito, E. Radicioni, R. De Oliveira, J. Dumarchez, N. Abgrall, P. Bene, A. Blondel, A. Cervera, D. Ferrer, F. Maschiocchi, E. Perrin, J.-P. Richeux, R. Schroeter, G. Jover, T. Lux, A.Y. Rodriguez, and F. Sanchez, *Bulk micromegas detectors for large area TPC applications* Nucl. Instrum. Methods A 574, 2007, pp 425432

[24] http://www.ideas.no

[25] E. Noschis, G. Anelli, G. Cervelli, M. Eraluoto, K. Kurvinen, R. Lauhakangas, L. Ropelewski, and W. Snoeys, *Protection circuit for the T2 readout electronics of the TOTEM experiment* Nucl. Instrum. Methods A 572, 2007, pp 378-381

[26] http://www.quickusb.com